Polar (In,Ga)N/GaN Quantum Wells: Revisiting the Impact of Carrier Localization on the "Green Gap" Problem

Daniel S.P. Tanner,[1] Philip Dawson,[2] Menno J. Kappers,[3] Rachel A. Oliver,[3] and Stefan Schulz[1,*]

[1] *Photonics Theory Group, Tyndall National Institute, University College Cork, Cork T12 R5CP, Ireland*
[2] *School of Physics and Astronomy, University of Manchester, Manchester M13 9PL, United Kingdom*
[3] *Department of Materials Science and Metallurgy, University of Cambridge, 27 Charles Babbage Road, Cambridge CB3 0FS, United Kingdom*

(Received 7 June 2019; revised manuscript received 16 January 2020; accepted 20 March 2020; published 27 April 2020)

We present a detailed theoretical analysis of the electronic and optical properties of *c*-plane InGaN/GaN quantum-well structures with In contents ranging from 5% to 25%. Special attention is paid to the relevance of alloy-induced carrier-localization effects to the "green gap" problem. Studying the localization length and electron-hole overlaps at low and elevated temperatures, we find alloy-induced localization effects are crucial for the accurate description of (In,Ga)N quantum wells across the range of In content studied. However, our calculations show very little change in the localization effects when moving from the blue to the green spectral regime; that is, when the internal quantum efficiency and wall-plug efficiencies reduce sharply, for instance, the in-plane carrier separation due to alloy-induced localization effects changes weakly. We conclude that other effects, such as increased defect densities, are more likely to be the main reason for the green-gap problem. This conclusion is further supported by our finding that the electron localization length is large, when compared with that of holes, and changes little in the In composition range of interest for the green-gap problem. Thus, electrons may become increasingly susceptible to an increased (point) defect density in green emitters and as a consequence the nonradiative-recombination rate may increase.

DOI: 10.1103/PhysRevApplied.13.044068

I. INTRODUCTION

Wurtzite InGaN/GaN quantum-well (QW) systems, grown along the polar *c* axis, have allowed the realization of optoelectronic devices that emit bright light over a wide spectral range, including emission at previously unattainable short wavelengths, with unprecedented efficiency [1–3]. However, the internal quantum efficiency (IQE) drops rapidly for emission wavelengths beyond the blue spectral range [4,5], as shown in Fig. 1. This effect is known as the "green gap" problem [5,6]. Given the dramatic reductions in energy use, and the associated reduction in CO_2 emission that would result from the development of all-LED white-light sources, using red, green, and blue LEDs [5], the understanding and circumvention of the green-gap problem is an urgent scientific and ecological objective. However, the origin of this phenomenon in (In,Ga)N-based emitters is still a matter of some debate. Focusing on *c*-plane (In,Ga)N/GaN QWs, the green-gap problem has been discussed on the basis of mainly three factors and their combined effect on the radiative- and nonradiative-recombination processes in these heterostructures.

The first of these factors is the decreasing material quality of (In,Ga)N/GaN QW systems with increasing In content [8–13]. To grow (In,Ga)N QWs emitting in the green spectral region, low growth temperatures are typically required to suppress In-atom desorption during growth and thus to achieve higher In contents [13]. The results obtained by Hammersley *et al.* [13] indicate that these low growth temperatures lead to increased (point) defect densities. Additionally, with increasing In content in the well, the lattice mismatch between the (In,Ga)N QW and the GaN barrier increases, which encourages stress relaxation through defect formation [8,9,11]. In general, defects and structural imperfections can serve to reduce the IQE by acting as nonradiative-recombination centers [9,14]. Some of these issues may be reduced by use of innovative growth techniques [15–17].

The second factor contributing to the green-gap problem is a property intrinsic to wurtzite *c*-plane (In,Ga)N/GaN QWs and also related to the increase in lattice-mismatch-induced strain with increasing In content. The increase in strain leads to an increase in the piezoelectric polarization-vector field inside the (In,Ga)N QW [18,19]. The resultant

*stefan.schulz@tyndall.ie

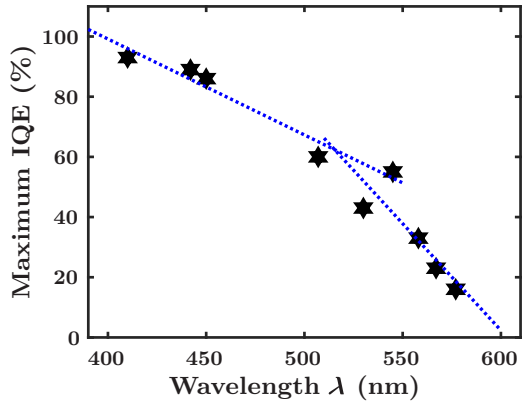

FIG. 1. Literature values for maximum internal quantum efficiency (IQE) as a function of the emission wavelength of *c*-plane (In,Ga)N/GaN systems [7].

intrinsic electrostatic built-in field leads to a separation of electron and hole wave functions along the growth direction. This effect is also known as the "quantum-confined Stark effect" (QCSE) [20]. Thus, the higher the In content, the larger the built-in field and the greater the reduction in the radiative-recombination rate due to the separation of charge carriers.

Taken together, the first factor (increased defect densities and nonradiative-recombination rates) and the second factor (reduction in radiative-recombination rate) will have a negative impact on the radiative optical properties of (In,Ga)N-based light emitters. As discussed above, these limitations will be worsened for higher In contents and thus emission in the green spectral region.

Very recently, a third factor contributing to the green-gap problem has received significant attention: carrier localization [21–26] due to (random) alloy fluctuations as well as structural inhomogeneities. Different groups have concluded that the alloy-related carrier-localization effects lead to an in-plane separation of electrons and holes in addition to the built-in field-induced effect described above [22,24,25,27].

Despite the large number of recent studies on this topic, there remains a significant degree of uncertainty as to which contribution is the dominant factor for the green gap problem, and accordingly how it may be best circumvented. Many studies impute the green gap primarily to an increased defect density [9,14,28]. Other studies focus on carrier-localization effects as the main source [25,26,29], and assume that nonradiative-recombination effects [such as defect-related Schockley-Read-Hall (SRH) recombination] are independent of the In content. These recent theoretical studies, wherein the green gap is attributed to material intrinsic carrier localization, result in a very pessimistic outlook in which the green gap cannot be closed by technological optimization of (In,Ga)N QWs [25,29]. This emphasis on localization as a negative feature of (In,Ga)N QWs is an interesting development, given that localization is widely regarded as the mechanism by which (In,Ga)N-based light-emitting devices, with their high defect densities, exhibit high efficiencies at all [30,31].

Given this ambiguity and disagreement in the literature, and the distinct approaches that each of these hypotheses suggest for further development of (In,Ga)N technologies, we revisit in this work the contentious issue of the origin of the green gap. Our results show that the localization characteristics in (In,Ga)N QWs do not change strongly from blue to green emitters, but rather change very little in this wavelength range. This lack of variation in localization effects has not been considered or discussed in work attributing the green-gap problem to carrier localization; only absolute numbers are discussed rather than focusing on changes in the carrier localization effects. Given that blue LEDs are very efficient, and that alloy-induced carrier-localization effects do not change dramatically between blue and green emitters, only slight changes to the *radiative*-recombination rate would be expected. This casts doubt on the assumption that the nonradiative recombination due to defects is constant and In content independent; if it were, the sharp drop in maximum IQE (see Fig. 1) and/or wall-plug efficiency (WPE), as we discuss below, would be difficult to explain. So contrary to the pessimistic conclusion that because of alloy-induced carrier-localization effects the green-gap problem cannot be solved, innovative growth techniques may allow its closure. For example, Haller *et al.* [32] recently suggested that by growing an (In,Ga)N underlayer before the QW layers, it is possible to getter nonradiative point defects to the underlayer, thereby increasing efficiency.

In this work we come to our conclusion by using an atomistic multiband tight-binding (TB) model that we first rigorously benchmark against experimental data for (In,Ga)N/GaN QWs emitting over a wide range of wavelengths. We study the photoluminescence (PL) peak energies, PL spectra widths and carrier localization lengths. Overall very good agreement between theory and experiment is found. This highlights that carrier-localization effects are accurately described by our model, thus providing a solid foundation for analyzing and predicting the importance of carrier localization for the green-gap problem.

This paper is organized as follows. In Sec. II A we introduce the theoretical framework. In Sec. II B structural properties of QW structures for the different In contents are discussed along with how these are treated in the modeling. The results of our calculations are presented in Sec. III. A theory-experiment comparison is given in Sec. III B. The analysis of the carrier localization length is presented in Sec. III C, followed by investigation of the electron-hole wave-function overlap as a function of In content in

Sec. III D. Our work is summarized in Sec. IV. Further details of the calculations and further supporting results are given in the Appendix.

II. THEORY AND QUANTUM-WELL SYSTEM

In this section we briefly review the theoretical framework used and the QW model systems studied. We start in Sec. II A with the theoretical framework and briefly introduce its main ingredients. In Sec. II B the supercell used in our calculations is described.

A. Theoretical framework

Our theoretical framework is based on an atomistic nearest-neighbor sp^3 TB model. The matrix elements of the TB Hamiltonian describing the binary materials are treated as free parameters, which are obtained by our fitting of the TB band structures to hybrid-functional-density-functional-theory (DFT) data [33]. While for In and Ga atoms the nearest-neighbor environment always consists of N atoms, N atoms can have variable numbers of In and Ga atoms as nearest neighbors. To determine the N-on-site energies in an alloy, weighted averages of the InN and GaN binary values are used, which is a widely used approximation in TB models for alloys [34–36]. Depending on, for instance, the reference DFT band structures, for the bulk systems different TB parameter sets may be obtained. This is similar to the situation one finds in multiband $\mathbf{k}\cdot\mathbf{p}$ models, where also different parameter sets are available in the literature [37]. In general, any TB parametrization should be tested and benchmarked against DFT or experimental data for *alloyed* systems. Such detailed comparison of our TB model in terms of the band-gap evolution in (In,Ga)N, (Al,In)N, and (Al,Ga)N alloys can be found in previously published work [33,38,39], showing that the model gives very good agreement with literature *ab initio* and experimental data. For such calculations also (local) strain and (local) built-in fields have to be taken into account.

To achieve an atomistic description of the strain field in a (In,Ga)N/GaN QW, we use a valence-force-field model [33]. By minimizing the valence-force-field elastic energy of the simulation supercell, we determine the relaxed atomic positions of the system. These then serve as input for the TB model, which accounts for the effect of strain on the electronic structure by an on-site correction to the TB matrix elements, the method for which is presented in Ref. [33].

In addition to (local) strain effects, (local) built-in polarization fields also affect the electronic and ultimately the optical properties of (In,Ga)N/GaN QWs [40–42]. In these systems, in particular, the strain-induced piezoelectric contribution plays a major role [19,20,40,43]. Macroscopic as well as local polarization effects are included in the calculation via the local polarization theory described in Ref. [33]. Ignoring local polarization fields may influence the carrier localization and such quantities as the full width at half maximum (FWHM) of the emission spectra. This is discussed in Refs. [44,45] in more detail.

By diagonalizing the constructed TB Hamiltonian matrix, we obtain the corresponding single-particle states. In previous work [31,41,46], we showed that for *c*-plane (In,Ga)N/GaN QWs at low temperatures, especially for well thicknesses exceeding 2.5 nm, Coulomb effects mainly lead to energetic shifts of the peak positions in the optical spectra but do not alter the localization characteristics significantly. Given that we are interested in carrier-localization effects and characteristics, ignoring Coulomb (excitonic) effects is a reasonable starting point for our analysis. To study the optical properties of *c*-plane (In,Ga)N/GaN QWs with different In content at low temperatures, we use single-particle states and energies in conjunction with Fermi's golden rule to obtain PL spectra [41,47]. For low-temperature and low-carrier-density studies, we calculate the dipole matrix elements for electron and hole ground states for each microscopic alloy configuration. Even though a large number of microscopically different configurations are used (see below), in Fermi's golden rule the δ function, describing the energy conservation, is replaced by a Lorentzian function with a standard deviation of 7 meV. For the composition range studied and for the number of microscopic configurations considered, this setting results generally in smooth low-temperature PL spectra, with the broadening of the δ function having a minimal effect on the width of the calculated spectra.

Finally, the supercell that contains the (In,Ga)N/GaN QW system and on which the calculations are performed has to be defined. This is the topic of the next section.

B. Quantum-well structures and simulation supercell

To study the importance of alloy-induced carrier localization for the green-gap problem, we choose to model *c*-plane (In,Ga)N/GaN QWs with In contents of 5%, 10%, 15%, and 25%, covering the blue-to-green spectral range. We simulate these QW systems using supercells with periodic boundary conditions that contain 81 920 atoms, corresponding to a system size of approximately $10 \times 9 \times 10\ \mathrm{nm}^3$. The details of the structures used in our theoretical study are labeled as "TBM" in Table I.

To compare and benchmark our results against literature values, we use Refs. [27,48,49], where the optical properties of a series of *c*-plane (In,Ga)N/GaN QWs were studied by theory and experiement. The theoretical results in Ref. [27] were obtained in the framework of a modified three-dimensional (3D) single-band effective-mass approach, further details of which may be found in Ref. [49]. The details of the QWs studied are also presented in Table I; experimental data from Graham *et al.* [48] are entitled "experiment," while the results of the modified 3D single-band effective-mass approximation are

TABLE I. Experimental and theoretical data on structural (In content, width L_w) and optical properties (PL peak energy, FWHM) of single (In,Ga)N/GaN QWs with diferent In content. The experimental data ("Experiment") are adapted from Ref. [48] (see also Ref. [49]). The results from calculations in the framework of a modified 3D single-band effective-mass approximation are denoted by "EMA" [27,49]. The results of the present study, using atomistic tight-binding theory, are labeled by "TBM."

Quantity	Experiment					Theory EMA					Theory TBM			
In content (%)	5 ± 3	12 ± 3	15 ± 3	19 ± 2	25 ± 2	5	12	15	19	25	5	10	15	25
Well width L_w (nm)	2.5 ± 0.3	2.7 ± 0.3	2.9 ± 0.3	3.2 ± 0.2	3.3 ± 0.2	2.5	2.7	2.9	3.2	3.3	2.85	2.9	3	3.5
PL peak energy (eV)	3.32	2.99	2.71	2.36	2.16	3.27	2.88	2.69	2.49	2.14	3.23	2.96	2.62	1.99
FWHM (meV)	23	62	76	56	61	34	50	58	69	75	35	59	84	93

labeled "EMA." Since our focus is on general trends with increasing In content, we do not aim for a direct one-to-one comparison with the structures reported in Ref. [48]. Such a one-to-one theory-experiment comparison would, in general, be difficult, given that the In fractions and well widths reported in Ref. [48] were determined by electron-energy-loss spectroscopy and high-resolution transmission electron microscopy, respectively, which result in large errors for the measured In contents and to a lesser degree for the well widths. For instance, for the system with the lowest In content, grown at 800 °C, the well width is 2.5 ± 0.3 nm and the In content is (5 ± 3)%. We therefore keep uncertainties in mind when comparing with data from Ref. [48].

For our atomistic theoretical framework, information on the In-atom distribution is also required. In the following we assume a random distribution of In atoms, which is consistent with experimental results, for instance, obtained by careful atom-probe-tomography studies [48,50–52]. We highlight that even the sample with 25% In content is not expected to deviate from a random In-atom distribution as the atom-probe analysis in Ref. [53] shows. Also, the same assumption about the random In-atom distribution was made by Watson-Parris *et al.* [27,49] in the modified 3D continuum model. Since several studies have revealed that the alloy microstructure significantly impacts the optical properties of *c*-plane (In,Ga)N QWs [22,23,27,41,54,55], we construct, for each In content, 175 different configurations with different random In-atom distributions. This allows us to obtain reliable statistical averages and to calculate quantities such as the FWHM of the PL spectra and thus to compare such data with experimental findings.

Using Fermi's golden rule to calculate, as detailed above, the low-temperature and low-carrier-density optical spectra in combination with the 175 different microscopic configurations, we find for all cases but the case with 25% In smooth PL spectra; for the system with 25% In, we still observe a slightly "noisy" PL spectrum. By use of more configurations, or a wider Lorentzian function for each PL peak resulting from the different microscopic configurations, this "noise" could be mitigated; however, to keep the settings consistent across the different In contents, such adjustments are not made. Thus, the predicted FWHM values for the 25%-In well should be regarded as a lower bound for this system. Since we want to study the electronic structure and the optical properties in detail and for different temperatures, we consider for higher temperatures and carrier densities not only ground states of each of the microscopic configurations but also excited states. Thus, we calculate for each of the 175 different configurations per In content 20 electron and 40 hole states. With this we are able to account for the fact that carriers will populate excited states at elevated temperatures.

As a last ingredient we introduce structural inhomogeneities in the theoretical description, namely, well-width fluctuations (WWFs) at the upper interface of the well [27,41,49]. Following the experimental and theoretical work in Refs. [27,41,49], these WWFs are described by disklike objects with a diameter of approximately 5 nm and a height of two monolayers. We stress that these objects allow now, in a spatially restricted region, the presence of In atoms in the GaN barrier. Given that we treat (In,Ga)N as a random alloy, the actual shape and form of these WWFs will vary and change from microscopic configuration to microscopic configuration. This situation is different when, for instance, compared with a continuum-based calculation, where a rigid object with constant size, shape and average In content would be introduced to describe a WWF.

Effects such as penetration of In atoms into the barrier, beyond the WWFs discussed above, are not included. Ignoring these effects is based on the following arguments given in the literature. First, it was recently shown that by a careful choice of the growth conditions this effect can be reduced [56]. While this In penetration effect could be expected to be of relevance for the samples in Ref. [48], in structures grown more recently this effect is expected to be less pronounced. Moreover, Watson-Parris [49] studied such a diffuse upper QW interface and concluded that this factor has no noticeable impact on carrier-localization effects. This stems from the fact that the distribution of the In atoms, when penetrating into the barrier, is homogeneous in the QW plane, while in the observed WWFs the In content is more noticeably concentrated. Thus, the impact of the WWFs on carrier-localization characteristics is much more pronounced than a diffuse upper interface. Finally, for a consistent comparison between the results of

our model here and those of the modified 3D single-band effective-mass model [27,49], the same basic assumptions about the structural properties are made. Following Ref. [27] and on the basis of the other considerations above, we exclude in our model In-atom penetration into the barrier, except for effects introduced by WWFs.

III. RESULTS

Having introduced the theoretical framework and the (In,Ga)N/GaN QW systems to which it is applied, we present in the following subsections the results of our calculations. In a first step, in Sec. III A, we give an overview of some general aspects of the electronic structure of *c*-plane (In,Ga)N/GaN QWs. Special attention is paid to carrier-localization effects. This analysis supports and underpins the findings of the following sections. In Sec. III B we use the experimental data extracted from Refs. [48,49] to benchmark our theoretical results across the In-content composition range from 5% to 25% and compare them also with theoretical data obtained by Watson-Parris *et al.* [27,49] (see above). In Sec. III C, we study carrier localization lengths as a function of the In content and temperature for a fixed carrier density. Our calculated values are compared with experimental data from Ref. [48] discussed in Sec. III B. Finally, in Sec. III D, the electron-hole wave-function overlaps are investigated. Attention is directed toward the contribution of the in-plane carrier separation to the reduction in the wave-function overlap with increasing In content. Secs. III C and III D shed light on the connection between carrier-localization effects and *changes* in the optical properties of (In,Ga)N/GaN QWs when the emission is pushed from the blue-wavelength regime to the green and orange parts of the spectrum.

A. General aspects of the electronic structure of *c*-plane (In,Ga)N/GaN quantum wells

Figure 2 shows isosurface plots of the electron $|\psi^e_{\rm GS}|^2$ (red) and hole $|\psi^h_{\rm GS}|^2$ (blue) ground-state (GS) charge densities for the microscopic configuration 13 of (In,Ga)N QWs with 10% In (left) and 15% In (right). The results are displayed for a side view, perpendicular to the wurtzite *c* axis, and a top view, along the wurtzite *c* axis. Several aspects of these plots are of interest for the results discussed below. First, the side view reveals a salient feature of *c*-plane (In,Ga)N QWs: the vertical separation of the electron and hole wave functions due to the built-in field. This significantly reduces the wave-function overlap. Second, for both systems we find strongly localized hole ground-state wave functions, revealing that random alloy fluctuations are sufficient to give rise to carrier-localization effects. This localization of hole states is observed across all configurations. For electrons we find that wave functions are localized by the WWFs. In general, and also as

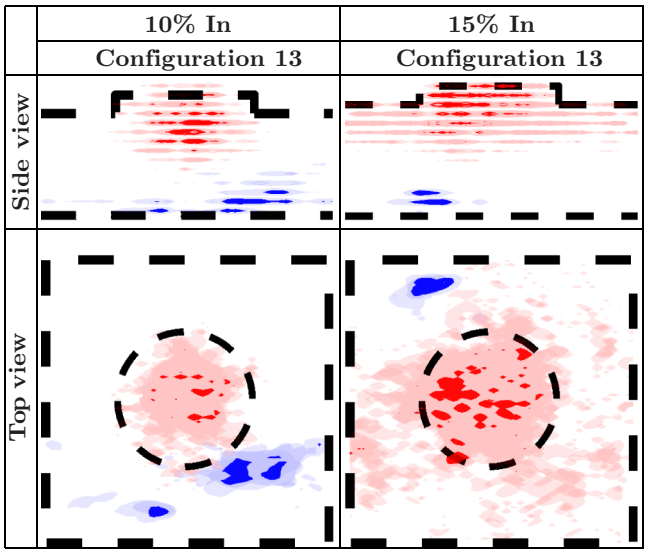

FIG. 2. Isosurface plots of electron (red) and hole (blue) ground-state charge densities. The light (dark) isosurfaces correspond to 15% (40%) of the respective maximum values. Results are given for configuration 13 for *c*-plane (In,Ga)N/GaN QWs with 10% In (left) and 15% In (right) in the well. The dashed lines indicate the QW interfaces. The results are shown for a side view (perpendicular to the *c* axis) and a top view (along the *c* axis).

in our previous results [31,41,46], the hole wave functions are more strongly localized than those of the electrons. We return to this point later when discussing quantitatively the electron and hole localization lengths.

Taking these two points together, our results show that in polar (In,Ga)N/GaN QW systems the interplay between random alloy fluctuations, WWFs, and electrostatic built-in field results in both an out-of plane separation and an in-plane separation of the carriers. This stems from the fact that holes do not necessarily localize below the WWF where the electrons are localized. We note that this in-plane carrier separation is also present in structures without WWFs, and as we discussed in previous studies, WWFs enhance, rather than produce this phenomenon [46]. The underling cause of the in-plane separation is that, being separated to opposite ends of the QW by the built-in field, electrons and holes each inhabit a different alloy or potential landscape, and those regions most energetically favorable for an electron to localize at the upper interface are mainly uncorrelated with those regions energetically favorable for the holes to localize at the lower interface (see Fig. 2). The finding of an in-plane spatial separation is consistent with theoretical work of Watson-Parris *et al.* [27], Auf der Maur *et al.* [22], and Jones *et al.* [23] It is also consistent with the pseudo-donor-acceptor-pair model introduced by Morel *et al.* [57] to explain time-resolved optical properties of *c*-plane (In,Ga)N/GaN

QWs. In Refs. [22,24,25], by assuming a constant defect-related nonradiative contribution, the in-plane separation or the combination with the built-in field is even regarded as the main driver behind the green-gap problem. However, before turning to this question in more detail, we first start by benchmarking our theory against experimental data across the In composition range and the resultant emission-wavelength range relevant to the green-gap problem. Our low-temperature experimental data indicate (see Table I) that 19% In and a well width of 3.2 ± 0.2 nm is enough to achieve emission in the spectral range relevant to the green-gap problem. In the theoretical study in Ref. [22], a well width of 3 nm and 30% In was required to push the emission wavelength to a comparable value; we note that these calculations were performed for emission at room temperature. Thus, the In content in the theoretical study in Ref. [22] is noticeably different from the In content in the experimental work in Ref. [48] (see Table I), while the well width is not vastly different. Therefore, a detailed theory-experiment comparison is important to ensure that the theoretical model describes key optical properties of realistic and experimentally relevant structures correctly before it is applied to analyze the impact of carrier localization on the green-gap problem.

B. Theory versus experiment: PL peak-position energies and FWHM values

The low-temperature and low-excitation-carrier-density optical properties of (In,Ga)N/GaN QWs presented in Ref. [48] provide an ideal starting point for comparing trends predicted by our theory for PL peak energies and FWHM values over a wide In composition range. In Table I, the optical and structural properties of the QW systems studied are presented and summarized. As discussed above, our aim is not to match structural properties or PL peak energies exactly. Rather we are interested in studying how the optical properties of polar (In,Ga)N/GaN QWs *change* with increasing In content and if we capture the main features of the measured spectra. From comparison of the theoretical and experimental data presented in Table I, our theory gives a good description of the PL peak energy with increasing In content. Furthermore, we find good agreement with the theoretical data from Refs. [27,49], which used a modified 3D EMA that also accounts for random alloy fluctuations.

In a second step, our calculated FWHM values are compared with both the experimental data [48] and the theoretical data [27,49] (see Table I). It is important to note that the experimental optical studies were performed at low temperatures T ($T = 6$ K) and low-excitation carrier densities, so it is reasonable to assume that occupation of excited (electron and hole) states is of secondary importance. Several features of this comparison are now of interest. Looking at Table I, we observe that over the composition range from 5% to 15% In (PL peak energies between approximately 2.6 eV and approximately 3.35 eV), our theoretical results for the FWHM are in good agreement with the experimental data from Graham *et al.* [48]. In this energy (wavelength λ, In content) range an increase in the FWHM with decreasing PL energy E_{PL} (increasing emission wavelength λ) is observed. The calculations from Refs. [27,49] in this energy or composition range always give lower numbers, except for the case with 5% In. Nevertheless, over the In-content range from 5% to 15% the trend of increasing FWHM values with decreasing PL peak energy (increasing In content) is also borne out by the EMA. We find good agreement between theory and experiment in terms of FWHM values *without* introducing In-clustering effects, in contrast to a recent study [58]. As indicated above, even for the higher-In-content samples, we do not find experimental evidence for clustering. Turning to the higher-In-content systems (In content more than 15%) and lower PL peak energies, $E_{\mathrm{PL}} < 2.7$ eV, we find both theoretical models predict a further increase of the FWHM. This is in contrast to the experimental data, which reveal a sudden drop in the FWHM in the energy range below 2.7 eV (samples with 19% and 25% In; see Table I). However, as we highlighted above, given that these single-QW systems were characterized by electron-energy-loss spectroscopy and high-resolution transmission electron microscopy, both nominal In content and well width may exhibit large error bars. Turning to the literature, recent results on multiple-QW structures at room temperature show that the FWHM increases at longer wavelength and lower PL peak energies [59]. Obviously, in these multiple-QW systems other factors such as well-to-well variations could play a role. Thus, future studies, ideally with single-QW samples with different In content, could target further careful optical and structural characterization of such systems to shed more light on our observed discrepancies between theory and experiment; such a detailed and refined investigation is beyond the scope of the present study.

Overall, the comparison shows that our theoretical framework gives a good description of several of the optical features of *c*-plane (In,Ga)N/GaN QWs across the In-content range relevant to the green-gap problem. Building on this, we now calculate carrier localization lengths as a function of the In content. This quantity was recently used to establish a connection between (hole) localization effects and the green gap [24,25].

C. Carrier localization length

Different approaches have been used in the literature to evaluate the carrier localization length. These include the inverse participation ratio (IPR) [60–62], the volume fraction [63], and the variance of the position operator [49]. Here we use the IPR to calculate wave-function

localization lengths. To define the IPR, we recall that the TB wave function ψ can be written as

$$\psi = \frac{1}{\sqrt{N}} \sum_{i}^{N} \sum_{\alpha} a_{i,\alpha} \phi_{i,\alpha}. \quad (1)$$

The index α denotes the orbital type (s, p_x, p_y, p_z) in our nearest-neighbor sp^3 TB model and the label i runs over the N lattice sites of the supercell ($N = 81\,920$). On the basis of Eq. (1), we can define the IPR as follows: [54]

$$I = \sum_{i}^{N} \left(\sum_{\alpha} |a_{i,\alpha}|^2 \right)^2 \Big/ \left(\sum_{i}^{N} \sum_{\alpha} |a_{i,\alpha}|^2 \right)^2. \quad (2)$$

For a Bloch (delocalized) state, we would have $I = 1/N$ [61]. Conversely, a localized state (only orbital contributions on the same lattice site k) would have $I = 1$. Given that a state with an IPR that is twice that of another state can be regarded as 2 times more localized, we can use the volume of a reference state to associate a given IPR with a length. In this we follow a procedure similar to that of Thouless [60], who defined a localization length l^{loc} of $a \times I^{-1/3}$ for a cubic lattice with lattice spacing a. However, we refine this procedure to account for the fact that we are dealing with a wurtzite crystal structure and more importantly with wurtzite QW systems that exhibit a built-in field. Therefore, we differentiate between the in-plane and out-of growth plane directions in these systems and go a step further than the isotropic localization length defined in other theoretical studies [24,49,63]. This treatment allows a closer comparison between our theory and experimental data that reports on in-plane hole localization lengths [48].

To calculate the out-of plane localization length of a given state ψ, we introduce the planar integrated probability density, $P(z_n)$:

$$P(z_n) = \sum_{k,l} |\psi(x_k, y_l, z_n)|^2, \quad (3)$$

where x_k and y_l are the in-plane (c-plane) coordinates and z_n denotes the nth layer along the c axis. This quantity represents a probability density per layer, where $P(z_n)$ gives the probability that the carrier described by state ψ will be found in the nth layer of the supercell, and $\sum_n^{N_z} P(z_n) = 1$, where N_z is the number of x-y planes in the system. From this one-dimensional probability density we may define an IPR value, $I_z = \sum_{z_m} [P(z_m)]^2$, and follow Thouless [60] to relate this to a length via the formula $l_z^{\text{loc}} = a_z \times I_z^{-1}$, where a_z is the average spacing between z layers in our relaxed supercells.

The in-plane localization length $l_{x\text{-}y}^{\text{loc}}$ can be calculated by building on the out-of plane length and a reference state.

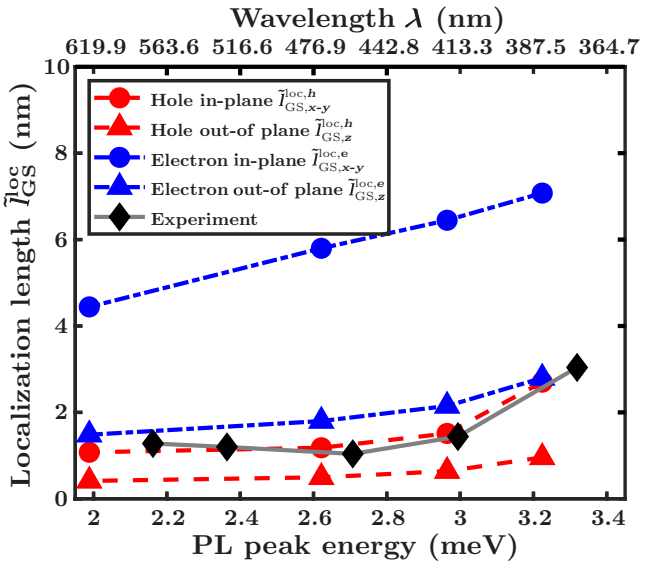

FIG. 3. Calculated average ground-state electron localization length $\tilde{l}^{\text{loc},e}_{\text{GS}}$ (red symbols) and hole localization length $\tilde{l}^{\text{loc},h}_{\text{GS}}$ (blue symbols) as a function of PL peak energy. The in-plane (out-of plane) localization length is given by the circles (triangles). The data are averaged over the 175 different microscopic configurations considered per In content. Experimental data are given by the black diamonds.

We do not go into the detail of the calculations here, but present them in the Appendix. Using this approach, we calculate the in-plane and out-of plane *average ground-state* localization lengths for electrons $\tilde{l}^{\text{loc},e}_{\text{GS}}(x)$ and holes $\tilde{l}^{\text{loc},h}_{\text{GS}}(x)$ by averaging over the 175 configurations for each In content x. The results are shown as a function of the calculated PL peak energies in Fig. 3. The top x axis gives the corresponding emission wavelength λ. Here and in subsequent localization-length plots, electron lengths are given in blue, and hole lengths are given in red; in-plane lengths are denoted by filled circles and out-of plane lenghts are denoted by filled triangles.

Figure 3 reveals three properties that are general across all quantities. First, the hole ground-state wave functions are more localized than those of the electrons in both the in-plane dimension and the out-of plane dimension; this reflects the behavior seen in Fig. 2 and is due to the larger effective mass of the holes. Second, we note that there is a noticeable difference between all in-plane and out-of plane localization lengths; this highlights inaccuracies that may be incurred by the use of an isotropic localization length approximation, as in previous studies [25,63]. Third, we highlight that all calculated localization lengths reduce with decreasing PL peak energy, but that the rate of decrease is different for different quantities.

Turning to the specifics for the holes first, we note the in-plane and out-of plane localization lengths change very little for emission energies below 3 eV. The situation is slightly different for electrons, at least for the in-plane

localization length. Here with increasing In content or wavelength the electron ground-state in-plane localization length decreases more strongly. We impute this to the strong impact that the combination of built-in field and WWF has on the ground-state electron wave function: as the field increases, the electron wave function is pushed more into the WWF and as a consequence is more laterally confined. We note two aspects of the QWs that affect this behavior: firstly the WWFs and secondly the increasing well width with increasing In content. Keeping the well width fixed between the systems with 15% In and 25% In at, for instance, $L_w = 3$ nm would reduce the QCSE in the 25%-In case. In addition if WWFs are then also absent, the electron localization length should increase compared with the data presented here; this in general would come into play for the higher-In-content regime, where WWFs are more important. We note also that very good agreement between our calculated hole in-plane localization lengths and data extracted experimentally from Huang-Rhys-factor measurements is achieved [48], adding further trust that carrier-localization effects are treated accurately in our modeling frame. Overall, this emphasizes the importance of benchmarking the theoretical model against experimental data so that carrier-localization effects are not overestimated or underestimated.

So far we have only calculated ground-state localization lengths. Such an analysis should be sufficient when comparing our results with low-temperature and low-carrier-density (below 10^{11} electron-hole pairs per square centimeter) experimental data [64]. With increasing temperatures and carrier densities, energetically-higher-lying states become important. To shed light on this, we calculate the mean localization length $\overline{l_\alpha^{\mathrm{loc},\lambda}}(x,T)$, with $\alpha = x$-y (in plane) or $\alpha = z$ (out of plane), for both electrons ($\lambda = e$) and holes ($\lambda = h$) for low temperatures T (here $T = 10$ K) and at room temperature ($T = 300$ K). All the following calculations are performed for a fixed sheet carrier density of 1.5×10^{12} cm^{-2}. We choose this carrier density to go beyond the low-carrier-density assumption, but at the same time to avoid entering the regime where emission from a higher-energy band is observed in experimental studies, which stems from saturation of localized (ground) states [64]. In future studies, higher-density regimes will be targeted. However, to analyze trends in the average localization length and to gain insight into the impact of excited states on this quantity, our present approach is a good starting point.

Therefore, using the calculated energy distribution of electron and hole states and Fermi-Dirac statistics, we calculate $\overline{l_\alpha^{\mathrm{loc},\lambda}}(x,T)$ via

$$\overline{l_\alpha^{\mathrm{loc},\lambda}}(x,T) = \frac{1}{N_C}\sum_{i=1}^{N_C}\sum_{j=1}^{N_\lambda} f^{\lambda}(E_{j,i},x,T)\, l_{\alpha j,i}^{\mathrm{loc},\lambda}(E_{j,i},x), \quad (4)$$

where f^{λ} denotes the Fermi-Dirac distribution for electrons ($\lambda = e$) or holes ($\lambda = h$), N_c is the total number of microscopic configurations ($N_c = 175$), and N_λ denotes the number of states ($N_e = 20$, $N_h = 40$). Given that our calculations show carrier-localization effects, and that the wave vector is in general not a good quantum number, f^{λ} is treated as in the case of a quantum-dot system with discrete energy levels and not a **k**-dependent energy dispersion [65]. In doing so, Eq. (4) allows us to obtain mean localization lengths at a given temperature T, carrier density, and In content x. Further information, including the evolution of the hole localization length with energy and In content, is given in the Appendix.

Our results as a function of the In content x in the well are shown in Fig. 4(a) for low temperatures ($T = 10$ K) and in Fig. 4(b) for room temperature ($T = 300$ K). Firstly,

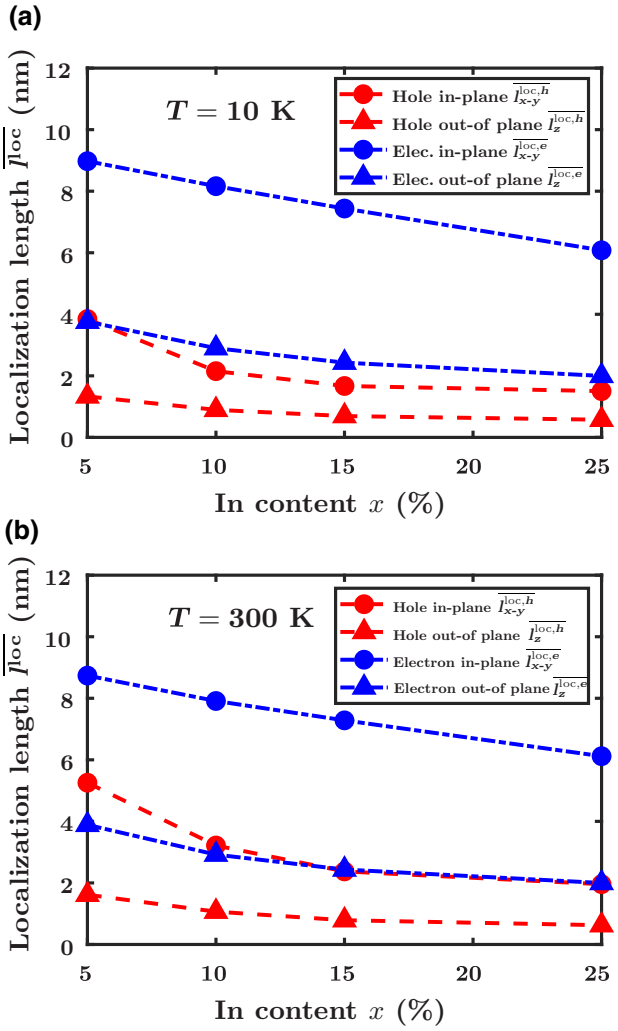

FIG. 4. In-plane (filled circles) and out-of plane (filled triangles) electron (blue) and hole (red) localization lengths at (a) $T = 10$ K and (b) $T = 300$ K. The sheet carrier density is 1.5×10^{12} cm^{-2}. Calculations are averaged over the 175 configurations.

we see that carrier-localization effects are still pronounced at higher carrier densities and temperatures. Comparing Fig. 3 with Fig. 4(a), we find that the increased carrier density leads to an increase in all localization lengths. In the case of the holes, this is attributable to the population of energetically-higher-lying localized states (see also the Appendix for more details), while for the electrons the increase in length may be due to occupation of states outside the WWF, which exhibit longer localization lengths due to the reduced (in-plane) confinement. In the absence of a WWF, a slight increase in the electron in-plane localization may be expected. Comparing Figs. 4(a) and 4(b), we note that increasing temperature has little effect on all the localization lengths other than the in-plane hole localization (filled red circles).

We note that $\overline{l_{x\text{-}y}^{\mathrm{loc},h}}$ for lower In contents is increased more than $\overline{l_{x\text{-}y}^{\mathrm{loc},h}}$ at higher In contents. For example, for the $T = 300$ K case, on going from 5% to 15% In content, $\overline{l_{x\text{-}y}^{\mathrm{loc},h}}$ is reduced by a factor of order 2.2, but on going from 15% to 25%, it is reduced by only a factor of order 1.2. Thus, the rate of change of the localization length with respect to In content is lower in the In content regime relevant to the green gap than it is at lower In-content regimes. The general trend of a smaller change in localization effects with increasing In content was also observed by other groups on different quantities. For instance, Piccardo *et al.* [55] observed that Urbach tail energies increase strongly in the In-content range from 6% to 11%, while for higher In contents the Urbach tail energy changes very little.

We highlight that the saturation of the hole localization length in the wavelength range relevant to the green gap (530–570 nm [13,22]) is an important result given that this quantity has generated interest as a first indicator of the deleterious effects of alloy-induced localization effects for the green-gap problem. Given that there is no sudden *change* in the hole localization length with increasing In content or wavelength, it is unlikely to explain the sudden decrease in IQE observed (see Fig. 1) when going from blue to green emitters.

To extend this discussion, we note further important factors. We recall that when (In,Ga)N/GaN QWs are grown with higher In contents, the growth temperature is lowered, resulting in an increase of the (point) defect density [10,12,66]. Point defects have been demonstrated to act as nonradiative-recombination centers, which can lead to a reduction in the nonradiative-recombination lifetimes [13, 67,68]. Thus, the holes, whose mean localization length remains small, may remain isolated from these defects, except for those that are localized near a defect. On the other hand, electrons, whose (in-plane) localization length is much larger, may now become increasingly susceptible to an increased (point) defect density. As a consequence, the nonradiative-recombination rate may be increased. This contrasts with Refs. [22,24], where a constant, In-content-independent nonradiative-recombination rate is assumed, and the reduction in device efficiency is mainly attributed to built-in field and carrier-localization effects due to random alloy fluctuations.

Finally, we note that if the carrier densities are increased further than those examined here, additional effects such as field screening will come into play, and the localization lengths of especially the electrons will further increase, as we showed in recent work [46]. The carriers will thus become more susceptible to defects, and the aforementioned conclusions will be strengthened. In the absence of WWFs, the electron localization length should increase and thus further support this conclusion. An interesting aspect of the above interpretation is the significant role played by the electrons, raising the question of whether it is the electrons that are the important carriers for the explanation of the green gap, rather than the holes, which have traditionally been targeted in this context.

Having discussed the electron and hole localization lengths, we turn now to the study of the wave-function overlaps. In particular, we focus on the importance of in-plane carrier separation for the green-gap problem.

D. Electron-hole wave-function overlap

To analyze how the electron-hole wave-function overlap changes with In content, we proceed as follows. In a first step, for each of the 175 different microscopic configurations per In content, the *modulus* electron-hole wave-function overlap, given by

$$\Omega^{eh}(n,m) = \sum_{i}^{N} (|\psi_{i,n}^{e}|^2 |\psi_{i,m}^{h}|^2)^{1/2} = \sum_{i}^{N} |\psi_{i,n}^{e}||\psi_{i,m}^{h}|, \quad (5)$$

is calculated between electron state ψ_n^e and hole state ψ_m^h. The sum runs over all the N lattice sites of the supercell. Our aim is to study the contribution of the in-plane carrier separation to the reduction of the total wave-function overlap; radiative-recombination lifetimes will be targeted in detail in future studies. Furthermore, we stress that our goal is to analyze the in-plane carrier separation *without* using a virtual crystal approximation (VCA) as a reference, as previous studies have done [22,23]. While a comparison between an atomistic model and a VCA model would allow us, in principle, to distinguish between in-plane-separation and out-of plane-separation contributions (carrier localization and built-in field), this comes at a cost: the magnitude and relative importance of the two different factors (built-in field and carrier localization), depend on how the parameters of the VCA calculations are determined (linear interpolation versus bowing parameters). Thus, the absolute numbers from a comparison with a VCA have to be treated with care. An approach that targets this question without a VCA will eliminate assumptions about

interpolating material parameters and remove therefore an extra layer of uncertainty. For these reasons the modulus wave-function overlap, Eq. (5), provides a coherent and consistent frame that does not suffer from assumptions made in a VCA reference frame, as we will discuss below in more detail. Also the above approach allows us in a simple manner to study the impact of the In content x on the spatial separation of wave functions in $In_xGa_{1-x}N/GaN$ QWs, both in and out of the growth plane. In general, more details about this approach and how we previously used it to gain insight into experimental observations such as a carrier mobility edge or the appearance of a high-energy emission band can be found in Refs. [64,69]. Furthermore, similar approaches have been used by other groups to study the optical properties of different nitride-based nanostructures [70,71].

Given that each electron and hole wave function is connected to a corresponding eigenenergy, one can also study an energy-resolved modulus wave-function overlap $\Omega^{eh}(E_n^e, E_m^h)$, where E_n^e is the electron eigenenergy and E_m^h is the hole eigenenergy of states n and m, respectively. In a second step, the overlaps $\Omega^{eh}(E_n^e, E_m^h)$ from the 175 different configurations are grouped together in energy bins of 30-meV width. An averaged energy-resolved modulus wave-function overlap $\widetilde{\Omega^{eh}}(E^e, E^h)$ is obtained by dividing the sum of the overlaps in an energy bin by the number of elements therein. To better compare the results from the different In contents, the data are always plotted with respect to corresponding conduction-"band" and valence-"band" edges.

The results of this analysis are displayed in Fig. 5, with the In content increasing from left to right. Three main results may be inferred from Fig. 5: (i) there is an overall decrease in electron and hole wave-function overlap with increasing In content (and well width); (ii) for a given system, the energy range over which electrons and holes have low overlaps with each other depends on the In content; (iii) the overlap depends more weakly on the electron energy than it does on the hole energy.

Result (i) reflects mainly an increasing strain-induced built-in field (which separates carriers perpendicular to the growth plane of the QWs; see Fig. 2) and alloy-fluctuation-induced carrier localization (which separates carriers in the growth plane; see Fig. 2) with In content, as discussed in Sec. III A. In our subsequent analysis, we disentangle the contribution of these two effects, as a function of the In content, to investigate the relevance of the alloy-induced in-plane carrier separation to the green-gap problem.

Result (ii) is a manifestation of an earlier-reported result [54] that not only does the strength of localization increase with In content but so too does the energy range over which it persists (see also the Appendix for further discussion and Ref. [54]). This may have interesting consequences for the green gap, or even efficiency droop: the carrier densities and temperatures required to saturate the localized states may be higher for higher-In-content QWs. We investigate this further below in the context of the green-gap problem.

Result (iii) arises from the fact that the electron localization length is large compared with the hole localization length and changes little when energetically-higher-lying states are populated, while the hole localization length increases as states deeper in the valence "band" are populated. More generally speaking, we note that this changing localization character and dependence of overlap on the energy of electrons and holes away from their respective conduction-"band" or valence-"band" edges is also reflected in experimental studies, for instance, in the appearance of a high-energy emission band with much shorter radiative-recombination times at low temperature ($T = 10$ K) [64].

While Fig. 5 gives the information on the evolution of the wave-function overlap with In content, it does not provide information about the density of states. Therefore, to gain further insight into all three aspects discussed above, in the next steps, we include the effects of temperature and carrier density on the wave-function overlaps, and investigate the specific contribution of the alloy-induced in-plane

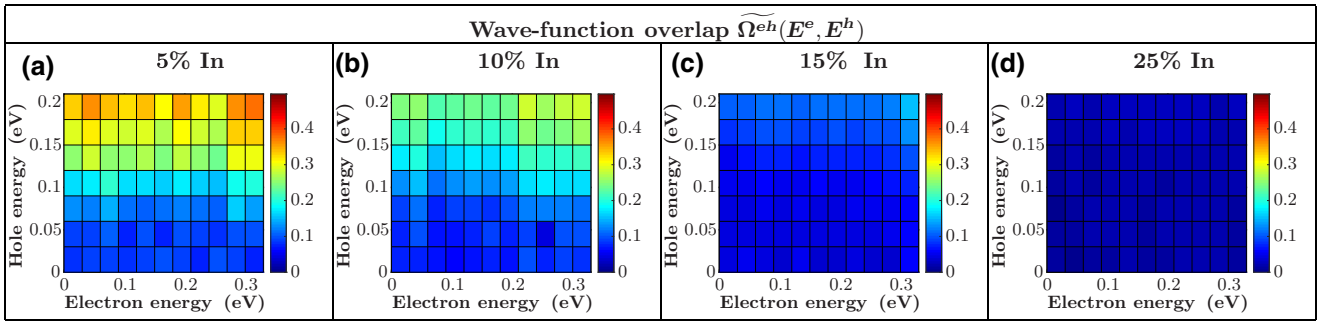

FIG. 5. Energy-resolved average modulus electron-hole wave-function overlap $\widetilde{\Omega^{eh}}(E^e, E^h)$ for the four different In contents considered: (a) 5%, (b) 10%, (c) 15%, and (d) 25%. The electron energies E^e are given on the x axis, while the hole energies E^h are given on the y axis. The results are obtained by averaging over 175 configurations per In content, where an energy bin size of 30 meV is used. The data are plotted with respect to the corresponding conduction-"band" and valence-"band" edges.

separation of carriers to the reduction of the electron-hole wave-function overlap, $\Omega^{eh}(E^e_n, E^h_m)$.

First, we introduce carrier-population effects due to higher temperatures and carrier densities as before using Fermi-Dirac statistics. Similarly to the localization length, $\overline{\Omega^{eh}}(T)$ is defined via

$$\overline{\Omega^{eh}}(T) = \frac{1}{N_c}\sum_{\alpha}^{N_c}\sum_{i,j} f^e(T, E^e_{i,\alpha}) f^h(T, E^h_{j,\alpha}) \Omega^{eh}(E^e_{i,\alpha}, E^h_{j,\alpha}), \tag{6}$$

where α denotes the configuration number of the $N_c = 175$ different microscopic configurations per In content. The electron and hole energies are denoted by $E^e_{i,\alpha}$ and $E^h_{j,\alpha}$, respectively. The factors f^e and f^h are the Fermi-Dirac functions for electrons and holes, respectively. The sheet carrier density n_s for all calculations is again 1.5×10^{12} cm^{-2}.

Next we examine the contribution of the in-plane separation to the reduction of $\overline{\Omega^{eh}}(T)$ at low ($T = 10$ K) and high ($T = 300$ K) temperatures. For the reasons discussed above, we study this question without using a VCA calculation. To achieve this unified description, we use the planar integrated probability density $P^{\lambda}_j(z_o)$, Eq. (3). From this quantity we can determine the planar integrated (modulus) overlap $\overline{\Omega^{eh}_P}(T)$. This quantity reflects what the overlap between two states would be if they were not separated from each other *in* the growth plane. Further discussion of this quantity and the details of its derivation are given in the Appendix. We may quantify the amount by which this is larger than $\overline{\Omega^{eh}}(T)$ or, more meaningfully, the amount by which $\overline{\Omega^{eh}}(T)$ is reduced by in-plane carrier separation using the following difference:

$$\delta\overline{\Omega_{\rm IP}}(T) = \frac{\overline{\Omega^{eh}_P}(T) - \overline{\Omega^{eh}}(T)}{\overline{\Omega^{eh}_P}(T)}. \tag{7}$$

Thus, $\delta\overline{\Omega_{\rm IP}}(T)$ represents the fractional reduction in the modulus overlap between electron and hole wave-functions due to their in-plane separation (i.e., due to alloy- and WWF-induced carrier-localization effects).

Figure 6 depicts the results of this analysis for the full overlap $\overline{\Omega^{eh}}(T)$ (black squares and circles) and the reduction in overlap due to in-plane separation $\delta\overline{\Omega^{eh}_{\rm IP}}(T)$ (red squares and circles). The squares denote $T = 10$ K (low-temperature) data, while the results at $T = 300$ K (room temperature) are given by the circles. Figure 6 reveals the general feature that with increasing In content (and well width) $\overline{\Omega^{eh}}(T)$ decreases, while $\delta\overline{\Omega^{eh}_{\rm IP}}(T)$ increases. The latter indicates an increase in in-plane carrier separation with increasing In content.

We now turn specifically to the evolution of the mean *full* overlap $\overline{\Omega^{eh}}(T)$ (black circles and squares), which

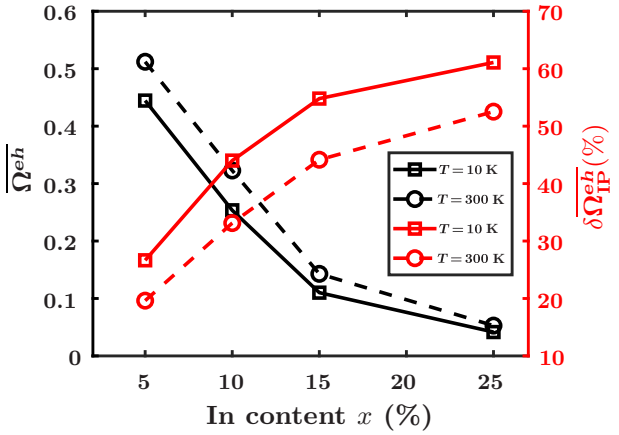

FIG. 6. The full mean modulus electron-hole wave-function overlap $\overline{\Omega^{eh}}$ is given in black; the in-plane contribution to the spatial separation $\delta\overline{\Omega^{eh}_{\rm IP}}$ (%) is given in red. Squares denote the results for $T = 10$ K, while the circles indicate the data for $T = 300$ K. The sheet carrier density n_s in the calculations is 1.5×10^{12} cm^{-2}.

gives a first indication of how the radiative-recombination rate changes with In content and temperature. Looking at the impact of temperature on the results, we see that increasing the temperature increases $\overline{\Omega^{eh}}(T)$ more for the lower-In-content systems than it does for the higher-In-content systems. This is a manifestation of the increasing energy range of localized states with increasing In content, as confirmed by Fig. 5. With increasing temperature, energetically-higher-lying states are populated; in the 5%-In case, carriers start to populate more-delocalised states sooner than in the 25% case, at the same carrier density. This highlights the importance of correctly describing the density of localized states to accurately model the radiative-recombination properties of these systems. It is also evident from this discussion that the indium content at which green emission is obtained in the model plays an important role. When having to use very high In content values in the calculations to push the emission wavelength into the green spectral part, the density of localized state may be overestimated, and as a consequence the importance of carrier localization for the green gap problem. This highlights again the importance of our initial theory-experiment benchmarking exercise.

Moreover, given that $\overline{\Omega^{eh}}(T)$ is related to the radiative-recombination rate, it can be seen that, for instance, for the 15%-In case, the radiative-recombination rate should increase with increasing temperature. Such an effect was observed in the experimental study of Nippert *et al.* [26] However, previous theoretical studies failed to explain this behavior [23] or had to include In-atom clustering effects [58]. Our results indicate the experimentally observed trend with temperature, thus highlighting that the

distribution of localized states is well described by our theoretical model.

Turning to the reduction in overlap due to in-plane carrier separation, $\delta\overline{\Omega_{\rm IP}^{eh}}(T)$, our data clearly show that this factor increases with increasing In content. While we find that indeed in-plane carrier separation contributes strongly to the overall reduction in electron-hole wave-function overlaps, and particularly so in the blue and green spectral regime and beyond, an examination of how this quantity changes with In content yields useful information as to the role played by in-plane carrier separation in the green-gap problem. For example, between 15% and 25% In, $\delta\overline{\Omega_{\rm IP}^{eh}}(x=0.25,T)-\delta\overline{\Omega_{\rm IP}^{eh}}(x=0.15,T)$ changes by less than 10%, whereas between 5% and 10% In, a much-more-significant change in $\delta\overline{\Omega_{\rm IP}^{eh}}(x=0.15,T)-\delta\overline{\Omega_{\rm IP}^{eh}}(x=0.05,T)$ of approximately 25% is observed. Examining thus the changes in the contribution of in-plane carrier separation to the wave-function overlap, we find little difference between the highly efficient blue emitters and those emitting in the green region and beyond. This can be attributed to the situation that the distribution of localized states with energy is not vastly different between the 15% and 25% In system over the ranges of temperature and carrier density considered. A further discussion is given in the Appendix. We point out that such a small change in carrier-localization effects in the higher-In-content regime was also observed by other groups on other quantities such as Urbach tail energies [55].

Finally, we note again that the argument of a smaller change in $\delta\overline{\Omega_{\rm IP}^{eh}}$ for higher In contents, when compared with the lower-In-content systems, would only be strengthened when the well width is kept fixed for different In contents and when WWFs are ignored. This again goes back to the situation that especially for the higher-In-content systems the QCSE is reduced when, for instance, a constant well width of, for example, 3 nm is assumed. Thus, for the higher-In-content system (25% In) the overall wave-function overlap should increase compared with the data presented for this system. Secondly, if we ignore the WWFs and reduce the QCSE by reducing the well width of the 25%-In structure chosen here, so that it is similar to the 15% case, the in-plane carrier localization of electrons will be reduced, which yields a reduction of the in-plane carrier separation between electrons and holes. This will lead to an overall reduction of $\delta\overline{\Omega_{\rm IP}^{eh}}$ and an even smaller change in $\delta\overline{\Omega_{\rm IP}^{eh}}$ in the In-content range from 15% to 25% when WWFs are removed and the same well width (e.g., 3 nm) is assumed.

Taking our results all together, they cast doubt on the idea that the observed slight change in $\delta\overline{\Omega_{\rm IP}^{eh}}$ with In content in the longer-wavelength regime is the fundamental origin of the green-gap problem. In other words, if the in-plane carrier separation presents a significant problem for the efficiency of (In,Ga)N-based light emitters, one could expect the drop in efficiency to be between the near-UV and the blue spectral range, with blue and green being almost equally efficient or inefficient. However, this is not observed in practice.

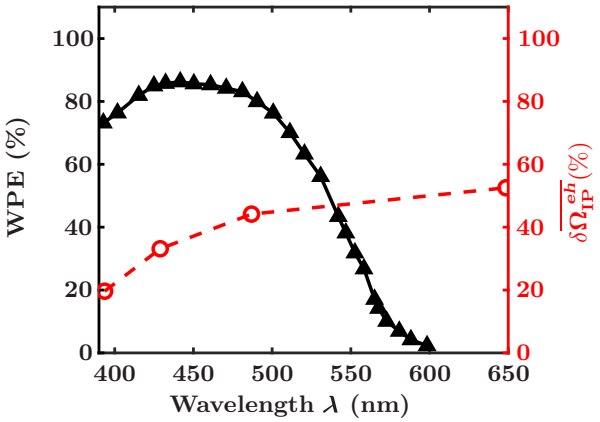

FIG. 7. Literature WPEs (black stars) of (In,Ga)N QW systems as a function of the emission wavelength [72]. The calculated reduction in wave-function overlap due to in-plane carrier-separation effects is given by the open red circles.

To further illustrate this point, we plot $\delta\overline{\Omega_{\rm IP}^{eh}}(T)$ against experimental literature data on peak WPEs of (In,Ga)N/GaN QW structures operating in the blue-to-green spectral region. The experimental WPEs (filled black triangles) are shown in Fig. 7 as a function of the emission wavelength. The data are extracted from Ref. [72]. The black line serves as a guide for the eye. For comparison we also plot $\delta\overline{\Omega_{\rm IP}^{eh}}(T)$ at $T=300$ K as a function of the calculated emission wavelength λ of the (In,Ga)N/GaN QWs with different In contents. The PL peak energies originally calculated at low temperature ($T=0$ K) and given in Table I are adjusted by use of the correction [73,74]

$$E_{\rm PL}(T)=E_{\rm PL}(0)-\frac{\alpha T^2}{\beta+T}-\frac{\sigma^2}{k_B T^2} \tag{8}$$

to account for the fact that experimental data in general are obtained at room temperature ($T=300$ K). $E_{\rm PL}(T)$ denotes the energy of the PL peak energy at temperature T and $E_{\rm PL}(0)$ is the PL peak energy at $T=0$ K. The second term on the right-hand side corresponds to the temperature dependence of the band gap described by the Varshni equation [75], where α and β are parameters taken from Ref. [75]; a linear interpolation between InN and GaN values is used. The last term on the right-hand side of Eq. (8) accounts for thermal distribution of carriers between localized states. Here k_B is the Boltzmann constant and σ is connected to the redshift of the PL peak position with temperature (S-shaped temperature dependence) [16,73,74,76,77]. The S-shaped temperature dependence of the PL peak energies has two redshift regions and Eq. (8) can be used only for the high-temperature part;

that is, above the temperature of the maximum FWHM [74]. For σ we use values reported in the literature for (In,Ga)N/GaN QWs with In contents ranging from 11% to 23% [16,76,77]. For the 5%-In system studied, we use $\sigma = 10$ meV. Applying Eq. (8) with literature σ values allows us to obtain a first approximation of the emission energies at elevated temperatures T. Calculating σ values from our data or a full PL spectrum near room temperature is beyond the scope of the present study.

Starting our analysis with the peak WPEs (filled black triangles), we observe first that the WPE is approximately constant in the $\lambda = 420$–490 nm window. In contrast to this, a strong decrease in these values from a wavelength of approximately 490 nm to 580 nm is observed. Comparing this now with our calculated in-plane separation-induced overlap-reduction contribution, $\delta\overline{\Omega_{\mathrm{IP}}^{eh}}(T = 300\ \mathrm{K})$, we find that $\delta\overline{\Omega_{\mathrm{IP}}^{eh}}(T)$ increases more rapidly in the $\lambda = 400$–490 nm regime. However, this is the range in which the WPE is approximately constant. On the other hand, the opposite behavior for WPE and $\delta\overline{\Omega_{\mathrm{IP}}^{eh}}(T = 300\ \mathrm{K})$ is observed in the $\lambda > 490$ nm wavelength window, meaning that $\delta\overline{\Omega_{\mathrm{IP}}^{eh}}(T = 300\ \mathrm{K})$ shows only a slow increase with wavelength, while the WPE drops quickly. This is opposite to what would be expected if changes in the in-plane carrier separation were the main driver behind the green-gap problem. Our results suggest instead that, given the slow rate of change of $\delta\overline{\Omega_{\mathrm{IP}}^{eh}}$, that carrier localization, and the associated in-plane separation, plays a minor role in the drastic decrease in WPE. This indicates that effects other than carrier localization, such as SRH recomination [78] and Auger recombination [28], must contribute to the sharp reduction in WPE.

To investigate the connection between wave-function overlap and IQE, we follow the often-made approximation to scale bulk recombination rates with the electron and hole wave-function overlaps obtained from QW calculations [23,79]. The absolute numbers depend strongly on the input parameters chosen as well as their carrier-density, temperature, and defect-density dependence, but one may use such an approach for an initial analysis of the *reduction* in IQE when changing the properties of the SRH recombination. To do so we use the electron and hole wave-function-overlap values from Fig. 6 at $T = 300$ K for the 15%-In system ($\lambda \approx 490$ nm) and a value from an extrapolation to 20% In ($\lambda \approx 570$ nm), since on the basis of Fig. 1 this is the wavelength region in which the IQE strongly drops. Given that our estimates are for a low-carrier-density regime, we expect that Auger recombination is of secondary importance. Thus the IQE should basically be determined by competition between radiative and SRH nonradiative recombination. In a first step we keep the SRH recombination constant and wavelength independent, and use numbers given in Ref. [22]. For the radiative recombination we use the DFT values from Ref. [80] at room temperature and low carrier densities, and scale them with the electron and hole wave-function overlaps from Fig. 6. In doing so, we find a *reduction* in IQE when keeping the SRH wavelength independent of 10% between the systems emitting at wavelengths of approximately 490 nm (15% In) and approximately 570 nm (20% In). However, the reduction in IQE over the wavelength window from 500 to 575 nm is on the order of 40%, as seen in Fig. 1. When SRH recombination is increased significantly (by a factor on the order of 6–8) but all other values are kept the same in the calculations, we find an drop in IQE on the order of 35%. Recent DFT studies show that for (In,Ga)N emitters operating in the green spectral range the SRH recombination is on the order of a factor of 6 larger when compared with their blue counterparts [78]. Thus, our simplified estimation of the impact of SRH on the IQE indicates a similar trend as the DFT study in Ref. [78].

Furthermore, if carrier-localization effects were the origin of the green-gap problem, nonpolar (In,Ga)N/GaN QW systems should *not* exhibit this efficiency reduction for the following reasons [81,82]. With the macroscopic built-in field absent in these structures, the attractive Coulomb interaction between electrons and holes leads to exciton-localization effects observed both in theory and in experiment [31,42,83,84]. In a Hartree-type picture the in-plane separation between electrons and holes will be strongly reduced due to their attractive Coulomb interaction. However, as discussed by Monavarian *et al.* [82], nonpolar systems do not solve the green-gap problem. Obviously, nonpolar systems differ significantly in crystal quality from their polar counterparts. This indicates already that even when the in-plane carrier separation is strongly reduced in a nonpolar system compared with a polar system, the crystal quality is still very important.

While our calculations confirm that carrier-localization effects and thus the associated in-plane separation effects significantly contribute to the wave-function-overlap reduction in *c*-plane (In,Ga)N/GaN QWs, we do not find strong *changes* in this quantity with changing In content in the In-content range relevant for the green-gap problem. Thus, it cannot explain the sharp decrease in, for instance, WPE (see Fig. 7). We highlight again that previous theoretical studies, which assumed a constant defect-related nonradiative rate, attributed carrier localization to be the main driver behind the green-gap problem [25,29]. Our results favor other factors, such as increased point-defect densities in emitters operating in the green spectral region and thus In-content-*dependent* nonradiative-recombination pathways, e.g. SRH [78] or defect-assisted Auger recombination [28], to be the more likely explanation for the green-gap problem. A similar conclusion was recently drawn in Ref. [28], where it was suggested that reducing the (point) defect density could close the green gap.

IV. CONCLUSION

In this work we revisited the importance of carrier localization for the green-gap problem. While this topic has been targeted by different groups, there remains uncertainty about the primary source of this phenomenon, and thus the best route by which it may be circumvented. As discussed above, several studies impute the green gap primarily to an increased defect density [9,14,28], while other studies focus on carrier-localization effects as the main source of this effect [25,26,29].

To shed new light onto this fundamental question, we build our analysis of carrier-localization effects on an atomistic multiband TB model that we extensively benchmark against experimental data for (In,Ga)N/GaN QWs emitting over a wide range of wavelengths. These studies indicate that carrier-localization effects are accurately described by our model. Quantities such as in-plane carrier separation and carrier localization lengths, originating from random alloy fluctuations, for In contents between 5% and 25% are directly calculated in an atomistic frame without fitting to experimental data.

Equipped with this model, we show that carrier-localization effects in (In,Ga)N QWs do not change strongly when the In content in the well is varied between 15% and 25% and thus in the emission-wavelength range from blue to green. This feature of a small change in the localization effects with In content has not been considered or discussed in studies attributing the green-gap problem to carrier localization. In previous works, only absolute numbers relating to the impact of localization on optical properties at a particular In content were discussed, rather than focussing on *changes* in these effects as a function of In content; in addition these works had the built-in assumption that the defect density did not change with In content. Given that blue LEDs are very efficient and that the differences in alloy-induced carrier-localization effects do not change strongly between blue and green emitters, only slight changes to the radiative-recombination rate are expected. Thus, our findings cast doubt on the conclusion that the nonradiative recombination due to defects is constant and In content independent; given the small change of localization effects in the In content range relevant to the green-gap problem, the sharp decrease in wall-plug efficiency would not be observed unless some other quantity, such as defect densities and, for example, trap-assisted Auger recombination, increased sharply.

This leads to the conclusion that further factors, such as the connection between the long electron localization length and the increased defect density in the high-In-content regime, which could lead to reduced nonradiative carrier lifetimes, are more likely to be the driver behind the green-gap problem. Experimental studies point in the same direction, although the details of the underlying mechanisms could be somewhat different [13,14,28].

On the basis of this explanation, accounting for the importance of the carrier (electron) localization length and increasing (point) defect densities for the green-gap problem, we suggest different countermeasures. One such countermeasure is, for instance, the already-widely-used approach of underlayers [32,85,86]. It has been shown that by the use of underlayers the point-defect density can be reduced in QWs, which should then be beneficial for the green-gap problem. Furthermore, from the finding of relatively long electron localization lengths and the potential connection to the nonradiative-recombination rate, tailoring carrier-localization effects might be the way forward to close the green gap. Here, for instance, colocalization of carriers by introducing quantum-dot-like structures in (In,Ga)N/GaN QWs could be such an approach. This would not only have the benefit of reducing the electron localization length but would also enhance the electron-hole wave function overlap. Experimentally this might be achieved by tailoring the growth parameters (particularly the growth pressure) to induce the formation of nonrandom clusters in QWs that are not usually present (dot-in-well structures).

ACKNOWLEDGMENTS

This work was supported by Science Foundation Ireland, the Sustainable Energy Authority of Ireland (Projects No. 17/CDA/4789 and No. 13/SIRG/2210), and the UK Engineering and Physical Sciences Research Council (Grant No. EP/M010589/1).

APPENDIX

In this appendix we provide (i) additional information about the calculation of the in-plane carrier localization length and its evolution with energy and In content for holes and (ii) further details of the in-plane carrier-localization effects. In the following section, the in-plane carrier localization length is discussed. Subsequently we discuss the in-plane carrier separation in more detail.

1. Hole localization length

In the main text we discuss the calculation of the out-of plane carrier localization length. Here we provide information about the calculation of the in-plane localization length. To evaluate the in-plane localization length $l^{\mathrm{loc}}_{x\text{-}y}$, we assign a single value by use of a reference state and the underlying hexagonal crystal symmetry. We choose as our reference state the electron ground state of configuration 13 with 10% In in the well, which is shown in Fig. 2 (left). This choice is made on the basis that in the plane the electron is mainly localized within the WWF. We then associate this state with a cylindrical volume given by $V_{\mathrm{ref}} = \pi r^2_{\mathrm{ref}} h_{\mathrm{ref}}$, where r_{ref} is the radius of the WWF ($r_{\mathrm{ref}} \approx$ 2.5 nm) and $h_{\mathrm{ref}} = l^{\mathrm{loc}}_{z,\mathrm{ref}}$ is the out-of plane localization

length for the reference state. Then, using the fact that the ratios of volumes occupied by two states are the same as the inverse of the ratio of their IPRs, we obtain, for a given microscopic configuration n, the following expression for the in-plane localization length $l^{\mathrm{loc}}_{x\text{-}y}$ of a given state:

$$l^{\mathrm{loc}}_{x\text{-}y} = 2\sqrt{\left(\frac{I_{\mathrm{ref}}}{I}\right)\left(\frac{r^2_{\mathrm{ref}} l^{\mathrm{loc}}_{z_{\mathrm{ref}}}}{l^{\mathrm{loc}}_{z}}\right)}, \tag{A1}$$

where I_{ref} is the full IPR defined by Eq. (2) for our reference state discussed above (electron ground state of configuration 13; 10% In). The factor of 2 in Eq. (A1) is used to give the full length (diameter) of the circular geometry assumed here.

In the main text we focus on the mean carrier localization length. In the following we present a detailed study of the in-plane hole localization ($l^{\mathrm{loc},h}_{x\text{-}y}$); the out-of plane localization length for electrons and holes is mainly dominated by the built-in field. Furthermore, we saw in our previous work that variations in the electron IPRs are much smaller than those in the hole IPRs [54]. In what follows, we investigate the extent to which the hole in-plane localization length changes as states deeper into the valence "band" are considered, since this can give insight into or an indication of the distribution of localized states in the valence "band" (density of states).

To address this point, the in-plane localization length $l^{\mathrm{loc},h}_{x\text{-}y}$ is calculated for each of the 40 hole states in each of the 175 configurations per In-content system. To plot the data from different configurations as a function of energy, the results are collected in bins of size 30 meV and the average localization length per bin is calculated. A bin size of 30 meV is chosen so that it is not too large to mask any intrinsic features but not so small as to produce any empty energy bins. To compare the results between the different In contents easily, the data are always shown with respect to the respective valence-"band"-edge values.

The resulting energy-resolved hole in-plane localization lengths are displayed in Fig. 8. Independent of the In content, we observe that the hole in-plane localization length $l^{\mathrm{loc},h}_{x\text{-}y}$ increases with increasing energy (moving deeper into the valence "band"). However, over an energy range of approximately 60 meV there is not a huge difference in the hole localization length at each In content. At first glance this seems to be in contradiction with Fig. 3, where the average *ground-state* in-plane localization length $\tilde{l}^{\mathrm{loc},h}_{\mathrm{GS},x\text{-}y}$ is plotted and at 5% In ($E^{\mathrm{theory}}_{\mathrm{PL}} = 3.23$ eV) $\tilde{l}^{\mathrm{loc},h}_{\mathrm{GS},x\text{-}y}$ is larger than in the 25%-In case ($E^{\mathrm{theory}}_{\mathrm{PL}} = 1.99$ eV). It is important to note that in Fig. 3 just *averages over the ground-state values* are taken; this ignores any spread in the corresponding hole ground-state energies. Figure 8 shows an *energy-resolved* in-plane localization length $l^{\mathrm{loc},h}_{x\text{-}y}(E)$. Therefore, one can find hole states that are as strongly localized

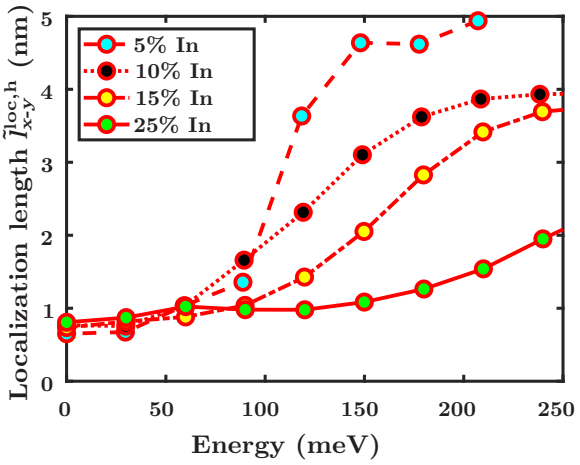

FIG. 8. Distribution of in-plane hole localization length $\tilde{l}^{\mathrm{loc},h}_{x\text{-}y}$ with respect to the valence-"band" edge for different In contents. The calculations use a bin size of 30 meV. Forty hole states per microscopic configuration are calculated. The binning is done over the 175 configurations.

in the 5%-In case as in the 25%-In case over the same energy range from the respective valence-"band" edge. However, the density of these strongly localized states increases significantly with increasing In content. We discussed this feature previously [54], when studying IPRs of electronic states as a function of the state number in c-plane (In,Ga)N/GaN wells with different In contents. Furthermore, Fig. 8 reveals that the energy region over which strong localization exists increases with increasing In content. For instance, while in the 5%-In case (filled blue circles, dashed line) the in-plane localization length starts to sharply increase at an energy of around 90 meV, for the 25%-In case (filled green circles, solid line) we do not start to see any such increase of the in-plane localization length until hole energies exceed 150 meV.

2. Wave-function overlap and in-plane carrier localization

In the main text we present the contribution of in-plane separation to the reduction in the wave-function overlap. Here we provide the derivation of this quantity, and detailed results underlying the mean values presented.

To obtain $\delta\overline{\Omega^{eh}_{\mathrm{IP}}}$, we begin with the planar integrated probability density $P^{\lambda}_{j}(z_o)$ of Eq. (3), which describes the one-dimensional probability density along the c axis. We can use $P^{\lambda}_{j}(z_o)$ to calculate the planar integrated (modulus) overlap $\Omega^{eh}_{P}(n,m)$ via

$$\Omega^{eh}_{P}(n,m) = \sum_{o}[P^{e}_{n}(z_o)P^{h}_{m}(z_o)]^{1/2}. \tag{A2}$$

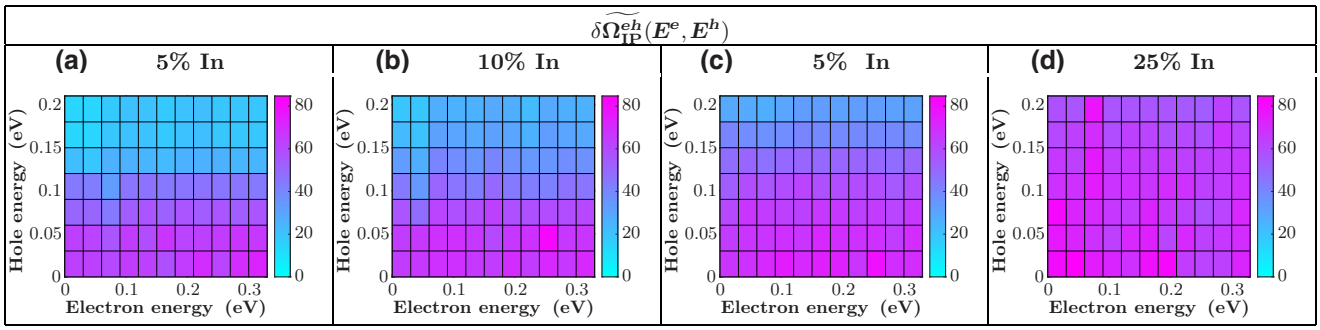

FIG. 9. Contribution $\delta\widetilde{\Omega}^{eh}_{\rm IP}$ (in percent) of the in-plane electron-hole separation to the electron and hole wave-function separation in the (In,Ga)N/GaN QWs considered with In contents of (a) 5%, (b), 10% (c) 15%, and (d) 25%. Electron energies E^e are given on the x axis and hole energies E^h are given on the y axis. Energies are plotted with respect to conduction-"band" and valence-"band" edges. The results are obtained by averaging over the 175 configurations per In content, where an energy bin size of 30 meV is chosen for both electrons and holes.

This quantity is sensitive only to the extent to which an electron wave function and a hole wave function reside in the same plane, irrespective of whether or not they occupy the same position in that plane. This is because, on the basis of Eq. (A2), the in-plane extent of the charge density is summed up into one value per plane. Consequently, all calculations are performed in the same frame containing the same microstructure, local strain, and built-in field fluctuations as the full-overlap calculations discussed above. The calculated planar integrated overlaps $\Omega^{eh}_P(n,m)$ can again be expressed in terms of electron energies E^e_n and hole energies E^h_m and an averaged value, denoted by $\widetilde{\Omega}^{eh}_P(E^e,E^h)$, which is obtained in the same manner as before for $\widetilde{\Omega}^{eh}(E^e,E^h)$ and discussed in the main text.

To quantify the amount by which this is larger than $\Omega^{eh}(E^e_n,E^h_m)$ or, more meaningfully, the amount by which $\Omega^{eh}(E^e_n,E^h_m)$ is reduced by in-plane carrier separation, we use the following metric:

$$\delta\widetilde{\Omega}_{\rm IP}(E^e,E^h)=\frac{\widetilde{\Omega}^{eh}_P(E^e,E^h)-\widetilde{\Omega}^{eh}(E^e,E^h)}{\widetilde{\Omega}^{eh}_P(E^e,E^h)}. \qquad \text{(A3)}$$

Figure 9 displays $\delta\widetilde{\Omega}_{\rm IP}(E^e,E^h)$ as a function of the electron and hole energies with respect to the respective conduction-"band" and valence-"band" edges.

It is apparent from Fig. 9 that in-plane separation strongly impacts the electron-hole overlaps, with percentage reductions in the overlap of up to around 80% seen for all In contents. Consistent with our results presented above for the localization lengths, the magnitude and energy range of this reduction increase with In content. For each In content, $\delta\widetilde{\Omega}_{\rm IP}(E^e,E^h)$ decreases with the distance from the valence-"band" and conduction-"band" edges, and decreases faster for lower In contents than for higher In contents. Again, the more-delocalized and unchanging nature of the electron states is evidenced by the relative insensitivity of $\delta\widetilde{\Omega}_{\rm IP}(E^e,E^h)$ to the electron energy E^e when compared with the hole energy E^h.

This significant impact of in-plane separation on the electron-hole overlap is consistent with previous studies that highlighted the negative impact of carrier localization and in-plane separation [22,24,25]. However, as pointed out earlier, it is important to study *changes* in this quantity between blue- and green-emitting systems if we wish to determine its relevance to the green-gap problem. If carrier localization and the associated in-plane separation were the main driver behind the green-gap problem, then a strong increase in $\delta\widetilde{\Omega}_{\rm IP}(E^e,E^h)$ should be evident when going from the 15%-In system to the 25%-In system.

Comparing the 15%-In system and the 25%-In system, we note that differences are indeed apparent on the high-energy side of Figs. 9(c) and 9(d), but on the low-energy side these differences are less marked. The question of the importance of these differences in these energy regimes is targeted in the main text.

Finally, to obtain $\delta\overline{\Omega_{\rm IP}}(T)$, we combine Eqs. (A2) and (6); the mean planar integrated overlap $\overline{\Omega^{eh}_P}(T)$ is obtained similarly; via Eq. (A3) the reduction in $\overline{\Omega^{eh}}(T)$ due to alloy-induced in-plane separation, $\delta\overline{\Omega^{e,h}_{\rm IP}}(T)$, at a given carrier density and as a function of temperature, is calculated.

[1] F. A. Ponce and D. Bour, Nitride-based semiconductors for blue and green light emitting devices, Nature **386**, 351 (1997).

[2] I. Akasaki and H. Amano, Breakthroughs in improving crystal quality of GaN and invention of the p-n junction blue-light-emitting diode, Jpn. J. Appl. Phys. **45**, 9001 (2006).

[3] S. Nakamura, T. Mukai, M. Senoh, S. Nagahama, and N. Iwasa, $In_xGa_{1-x}N/In_yGa_{1-y}N$ superlattices grown on GaN films, J. Appl. Phys. **74**, 3911 (1993).

[4] T. Mukai, M. Yamada, and S. Nakamura, Characteristics of InGaN-based uv/blue/green/amber/red light-emitting diodes, Jpn. J. Appl. Phys. **38**, 3976 (1999).

[5] C. J. Humphreys, Solid-state lighting, MRS Bull. **33**, 459 (2008).

[6] M. R. Krames, O. B. Shchekin, R. Mueller-Mach, G. O. Mueller, L. Zhou, G. Harbers, and M. G. Craford, Status and future of high-power light-emitting diodes for solid-state lighting, J. Disp. Technol. **3**, 160 (2007).

[7] S. Y. Karpov, Light-emitting diodes for solid-state lighting: Searching room for improvements, Proc. SPIE 9768, 9768 (2016).

[8] M. H. Crawford, Leds for solid-state lighting: Performance challenges and recent advances, IEEE J. Sel. Top. Quantum Electron. **15**, 1028 (2009).

[9] T. Langer, H. Jönen, A. Kruse, H. Bremers, U. Rossow, and A. Hangleiter, Strain-induced defects as nonradiative recombination centers in green-emitting GaInN/GaN quantum well structures, Appl. Phys. Lett. **103**, 022108 (2013).

[10] A. Armstrong, T. A. Henry, D. D. Koleske, M. H. Crawford, and S. R. Lee, Quantitative and depth-resolved deep level defect distributions in InGaN/GaN light emitting diodes, Opt. Express **20**, A812 (2012).

[11] F. C.-P. Massabuau, M. J. Davies, F. Oehler, S. K. Pamenter, E. J. Thrush, M. J. Kappers, A. Kovacs, T. Williams, M. A. Hopkins, C. J. Humphreys, P. Dawson, R. E. Dunin-Borkowski, J. Etheridge, D. W. E. Allsopp, and R. A. Oliver, The impact of trench defects in InGaN/GaN light emitting diodes and implications for the "green gap" problem, Appl. Phys. Lett. **105**, 112110 (2014).

[12] A. Uedono, S. Ishibashi, N. Oshima, R. Suzuki, and M. Sumiya, Point defect characterization of Group-III nitrides by using monoenergetic positron beams, ECS Trans. **61**, 19 (2014).

[13] S. Hammersley, M. J. Kappers, F. C. P. Massabuau, S.-L. Sahonta, P. Dawson, R. A. Oliver, and C. J. Humphreys, Effects of quantum well growth temperature on the recombination efficiency of InGaN/GaN multiple quantum wells that emit in the green and blue spectral regions, J. Appl. Phys. **107**, 132106 (2015).

[14] T. Langer, A. Kruse, F. A. Ketzer, A. Schwiegel, L. Hoffmann, H. Jönen, H. Bremers, U. Rossow, and A. Hangleiter, Origin of the "green gap": Increasing nonradiative recombination in indium-rich GaInN/GaN quantum well structures, Phys. Status Solidi C **8**, 2170 (2011).

[15] A. M. Armstrong, B. N. Bryant, M. H. Crawford, D. D. Koleske, S. R. Lee, and J. J. Wierer, Defect-reduction mechanism for improving radiative efficiency in InGaN/GaN light-emitting diodes using InGaN underlayers, J. Appl. Phys. **117**, 134501 (2015).

[16] Y. Zhu, T. Lu, X. Zhou, G. Zhao, H. Dong, Z. Jia, X. Liu, and B. Xu, Effect of hydrogen treatment temperature on the properties of InGaN/GaN multiple quantum wells, Nanoscale Res. Lett. **12**, 321 (2017).

[17] A. Tian, J. Liu, L. Zhang, Z. Li, M. Ikeda, S. Zhang, D. Li, P. Wen, F. Zhang, Y. Cheng, X. Fan, and H. Yang, Green laser diodes with low threshold current density via interface engineering of InGaN/GaN quantum well active region, Opt. Express **25**, 415 (2017).

[18] O. Ambacher, J. Majewski, C. Miskys, A. Link, M. Hermann, M. Eickhoff, M. Stutzmann, F. Bernardini, V. Fiorentini, V. Tilak, B. Schaff, and L. F. Eastman, Pyroelectric properties of Al(In)GaN/GaN hetero- and quantum well structures, J. Phys.: Condens. Matter **14**, 3399 (2002).

[19] S. K. Patra and S. Schulz, Electrostatic built-in fields in wurtzite III-N nanostructures: Impact of growth plane on second-order piezoelectricity, Phys. Rev. B **96**, 155307 (2017).

[20] A. D. Andreev and E. P. O'Reilly, Optical transitions and radiative lifetime in GaN/AlN self-organized quantum dots, Appl. Phys. Lett. **79**, 521 (2001).

[21] T.-J. Yang, R. Shivaraman, J. S. Speck, and Y.-R. Wu, The influence of random indium alloy fluctuations in indium gallium nitride quantum wells on the device behavior, J. Appl. Phys. **116**, 113104 (2014).

[22] M. Auf der Maur, A. Pecchia, G. Penazzi, W. Rodrigues, and A. Di Carlo, Efficiency Drop in Green InGaN/GaN Light Emitting Diodes: The Role of Random Alloy Fluctuations, Phys. Rev. Lett. **116**, 027401 (2016).

[23] C. M. Jones, C.-H. Teng, Q. Yan, P.-C. Ku, and E. Kioupakis, Impact of carrier localization on recombination in InGaN quantum wells and the efficiency of nitride light-emitting diodes: Insights from theory and numerical simulations, Appl. Phys. Lett. **111**, 113501 (2017).

[24] S. Y. Karpov, Carrier localization in InGaN by composition fluctuations: Implications to the green gap, Photonics Res. **5**, A7 (2017).

[25] S. Y. Karpov, Effect of carrier localization on recombination processes and efficiency of InGaN-based LEDs operating in the "green gap", Appl. Sci. **8**, 818 (2018).

[26] F. Nippert, S. Y. Karpov, G. Callsen, B. Galler, T. Kure, C. Nenstiel, M. R. Wagner, M. Straßburg, H.-J. Lugauer, and A. Hoffmann, Temperature-dependent recombination coefficients in InGaN light-emitting diodes: Hole localization, auger processes, and the green gap, Appl. Phys. Lett. **109**, 161103 (2016).

[27] D. Watson-Parris, M. J. Godfrey, P. Dawson, R. A. Oliver, M. J. Galtrey, M. J. Kappers, and C. J. Humphreys, Carrier localization mechanisms in $In_xGa_{1-x}N/GaN$, Phys. Rev. B **83**, 115321 (2011).

[28] A. David, N. G. Young, C. A. Hurni, and M. D. Craven, Quantum Efficiency of III-Nitride Emitters: Evidence for Defect-Assisted Nonradiative Recombination and its Effect on the Green Gap, Phys. Rev. Appl. **11**, 031001 (2019).

[29] M. Auf Der Maur and S. Yu Karpov, Getting to grips with the green gap, Compd Semicond. **23**, 28 (2017).

[30] S. F. Chichibu, A. Uedono, T. Onuma, B. A. Haskell, A. Chakraborty, T. Koyama, P. T. Fini, S. Keller, S. P. DenBaars, J. S. Speck, U. K. Mishra, S. Nakamura, S. Yamaguchi, S. Kamiyama, H. Amano, I. Akasaki, J. Han, and T. Sota, Origin of defect-insensitive emission probability in in-containing (Al, In, Ga)N alloy semiconductors, Nat. Mater. **5**, 810 (2006).

[31] P. Dawson, S. Schulz, R. A. Oliver, M. J. Kappers, and C. J. Humphreys, The nature of carrier localisation in polar and nonpolar InGaN/GaN quantum wells, J. Appl. Phys. **119**, 181505 (2016).

[32] C. Haller, J.-F. Carlin, G. Jacopin, D. Martin, R. Butte, and N. Grandjean, Burying non-radiative defects in ingan underlayer to increase InGaN/GaN quantum well efficiency, Appl. Phys. Lett. **111**, 262101 (2017).

[33] M. A. Caro, S. Schulz, and E. P. O'Reilly, Theory of local electric polarization and its relation to internal strain: Impact on the polarization potential and electronic properties of group-III nitrides, Phys. Rev. B **88**, 214103 (2013).

[34] E. P. O'Reilly, A. Lindsay, S. Tomic, and M. Kamal-Saadi, Tight-binding and $\mathbf{k}\cdot\mathbf{p}$ models for the electronic structure of Ga(In)NAs and related alloys, Semicond. Sci. Technol. **17**, 870 (2002).

[35] Z. Q. Li and W. Pötz, Electronic density of states of semiconductor alloys from lattice-mismatched isovalent binary constituents, Phys. Rev. B **46**, 2109 (1992).

[36] T. B. Boykin, N. Kharche, G. Klimeck, and M. Korkusinski, Approximate bandstructures of semiconductor alloys from tight-binding supercell calculations, J. Phys.: Condens. Matter **19**, 036203 (2007).

[37] S. K. Patra, O. Marquardt, and S. Schulz, Polar, semi- and non-polar nitride-based quantum dots: Influence of substrate orientation and material parameter sets on electronic and optical properties, Opt. Quant. Electron. **48**, 151 (2016).

[38] S. Schulz, M. A. Caro, L.-T. Tan, P. J. Parbrook, R. W. Martin, and E. P. O'Reilly, Composition-dependent band gap and band-edge bowing in AlInN: A combined theoretical and experimental study, Appl. Phys. Express **6**, 121001 (2013).

[39] C. Coughlan, S. Schulz, M. A. Caro, and E. P. O'Reilly, Band gap bowing and optical polarization switching in $Al_{1-x}Ga_xN$ alloys, Phys. Status Solidi B **252**, 879 (2015).

[40] D. P. Williams, A. D. Andreev, E. P. O'Reilly, and D. A. Faux, Derivation of built-in polarization potentials in nitride-based semiconductor quantum dots, Phys. Rev. B **72**, 235318 (2005).

[41] S. Schulz, M. A. Caro, C. Coughlan, and E. P. O'Reilly, Atomistic anaylsis of the impact of alloy and well width fluctuations on the electronic and optical properties of InGaN/GaN quantum wells, Phys. Rev. B **91**, 035439 (2015).

[42] S. Schulz, D. P. Tanner, E. P. O'Reilly, M. A. Caro, T. L. Martin, P. A. J. Bagot, M. P. Moody, F. Tang, J. T. Griffiths, F. Oehler, M. J. Kappers, R. A. Oliver, C. J. Humphreys, D. Sutherland, M. J. Davies, and P. Dawson, Structural, electronic, and optical properties of m-plane InGaN/GaN quantum wells: Insights from experiment and atomistic theory, Phys. Rev. B **92**, 235419 (2015).

[43] S. K. Patra, T. Wang, T. J. Puchtler, T. Zhu, R. A. Oliver, R. A. Taylor, and S. Schulz, Theoretical and experimental analysis of radiative recombination lifetimes in nonpolar InGaN/GaN quantum dots, Phys. Status Solidi B **254**, 1600675 (2017).

[44] M. Baranowski, L. Janicki, M. Gladysiewicz, M. Welna, M. Latkowska, J. Misiewicz, L. Marona, D. Schiavon, P. Perlin, and R. Kudrawiec, Direct evidence of photoluminescence broadening enhancement by local electric field fluctuations in polar InGaN/GaN quantum wells, Jpn. J. Appl. Phys. **57**, 020305 (2018).

[45] G. M. Christian, S. Schulz, S. Hammersley, M. J. Kappers, M. Frentrup, C. J. Humphreys, R. A. Oliver, and P. Dawson, Optical properties of c-plane InGaN/GaN single quantum wells as a function of total electric field strength, Jpn. J. Appl. Phys. **58**, SCCB09 (2019).

[46] D. S. P. Tanner, J. M. McMahon, and S. Schulz, Interface Roughness, Carrier Localization, and Wave Function Overlap in *c*-Plane (In, Ga)N/GaN Quantum Wells: Interplay of Well Width, Alloy Microstructure, Structural Inhomogeneities, and Coulomb Effects, Phys. Rev. Appl. **10**, 034027 (2018).

[47] S. Schulz, S. Schumacher, and G. Czycholl, Tight-binding model for semiconductor quantum dots with a wurtzite crystal structure: From one-particle properties to coulomb correlations and optical spectra, Phys. Rev. B **73**, 245327 (2006).

[48] D. M. Graham, A. Soltani-Vala, P. Dawson, M. J. Godfrey, T. M. Smeeton, J. S. Barnard, M. J. Kappers, C. J. Humphreys, and E. J. Thrush, Optical and microstructural studies of InGaN/GaN single-quantum-well structures, J. Appl. Phys. **97**, 103508 (2005).

[49] D. T. S. Watson-Parris, Carrier Localization in InGaN/GaN Quantum Wells, PhD Thesis, University of Manchester (https://www.escholar.manchester.ac.uk/uk-ac-man-scw:132844, 2011).

[50] B. Monemar, P. P. Paskov, J. P. Bergman, G. Pozina, V. Darakchieva, M. Iwaya, S. Kamiyama, H. Amano, and I. Akasaki, Photoluminescence in n-doped $In_{0.1}Ga_{0.9}N/In_{0.01}Ga_{0.99}N$ multiple quantum wells, MRS Internet J. Nitride Semicond. Res. **7**, 7 (2002).

[51] J. P. O'Neill, I. M. Ross, A. G. Cullis, T. Wang, and P. J. Parbrook, Electron-beam-induced segregation in InGaN/GaN multiple-quantum wells, Appl. Phys. Lett. **83**, 1965 (2003).

[52] T. M. Smeeton, M. J. Kappers, J. S. Barnard, M. E. Vickers, and C. J. Humphreys, Electron-beam-induced strain within InGaN quantum wells: False indium "cluster" detection in the transmission electron microscope, Appl. Phys. Lett. **83**, 5419 (2003).

[53] M. J. Galtrey, R. A. Oliver, M. J. Kappers, C. J. Humphreys, P. Clifton, D. Larson, D. Saxey, and A. Cerezo, Three-dimensional atom probe analysis of green- and blue-emitting $In_xGa_{1-x}N/GaN$ multiple quantum well structures, J. Appl. Phys. **104**, 013524 (2008).

[54] D. P. Tanner, M. A. Caro, E. P. O'Reilly, and S. Schulz, Random alloy fluctuations and structural inhomogeneities in c-plane $In_xGa_{1-x}N$ quantum wells: Theory of ground and excited electron and hole states, RSC Adv. **6**, 64513 (2016).

[55] M. Piccardo, C.-K. Li, Y.-R. Wu, J. S. Speck, B. Bonef, R. M. Farrell, M. Filoche, L. Martinelli, J. Peretti, and C. Weisbuch, Localization landscape theory of disorder in semiconductors. II. Urbach tails of disordered quantum well layers, Phys. Rev. B **95**, 144205 (2017).

[56] F. Massabuau, N. Piot, M. Frentrup, X. Wang, Q. Avenas, M. Kappers, C. Humphreys, and R. Oliver, X-ray reflectivity method for the characterization of InGaN/GaN quantum well interface, Phys. Status Solidi B **254**, 1600664 (2017).

[57] A. Morel, P. Lefebvre, S. Kalliakos, T. Taliercio, T. Bretagnon, and B. Gil, Donor-acceptor-like behavior of electron-hole pair recombinations in low-dimensional (Ga, In)N/GaN systems, Phys. Rev. B **68**, 045331 (2003).

[58] A. Di Vito, A. Pecchia, A. Di Carlo, and M. Auf der Maur, Impact of Compositional Nonuniformity in (In, Ga)N-Based Light-Emitting Diodes, Phys. Rev. Appl. **12**, 014055 (2019).

[59] Y. Robin, M. Pristovsek, H. Amano, F. Oehler, R. A. Oliver, and C. J. Humphreys, What is red? On the chromaticity orange-red InGaN/GaN based LEDs, J. Appl. Phys. **124**, 183102 (2018).

[60] D. J. Thouless, Electrons in disordered systems and the theory of localization, Phys. Rep. **13**, 93 (1974).

[61] F. Wegner, Inverse participation ratio in $2+\epsilon$ dimensions, Z. Physik B **36**, 209 (1980).

[62] H. Ludwig, E. Runge, and R. Zimmermann, Exact calculation of distributions for excitonic oscillator strength and inverse participation ratio in disordered quantum wires, Phys. Rev. B **67**, 205302 (2003).

[63] J. A. Chan, J. Z. Liu, and A. Zunger, Bridging the gap between atomic microstructure and electronic properties of alloys: The case of (In, Ga)N, Phys. Rev. B **82**, 045112 (2010).

[64] G. M. Christian, S. Schulz, M. J. Kappers, C. J. Humphreys, R. A. Oliver, and P. Dawson, Recombination from polar InGaN/GaN quantum well structures at high excitation carrier densities, Phys. Rev. B **98**, 155301 (2018).

[65] Y.-R. Wu, Y.-Y. Lin, H.-H. Huang, and J. Singh, Electronic and optical properties of InGaN quantum dot based light emitters for solid state lighting, J. Appl. Phys. **105**, 013117 (2009).

[66] E. Gür, Z. Zhang, S. Krishnamoorthy, S. Rajan, and S. A. Ringe, Detailed characterization of deep level defects in ingan schottky diodes by optical and thermal deep level spectroscopies, Appl. Phys. Lett. **99**, 092109 (2011).

[67] S. F. Chichibu, A. Uedono, T. Onuma, T. Sota, B. A. Haskell, S. P. DenBaars, J. S. Speck, and S. Nakamura, Limiting factors of room-temperature nonradiative photoluminescence lifetime in polar and nonpolar gan studied by time-resolved photoluminescence and slow positron annihilation techniques, Appl. Phys. Lett. **86**, 021914 (2005).

[68] T. Langer, H.-G. Pietscher, H. Bremers, U. Rossow, D. Menzel, and A. Hangleiter, Nonradiative recombination due to point defects in GaInN/GaN quantum wells induced by Ar implantation, Proc. SPIE 8625, 862522 (2013).

[69] W. E. Blenkhorn, S. Schulz, D. S. P. Tanner, R. A. Oliver, M. J. Kappers, C. J. Humphreys, and P. Dawson, Resonant photoluminescence studies of carrier localisation in c-plane InGaN/GaN quantum well structures, J. Phys.: Condens. Matter **30**, 175303 (2018).

[70] O. Marquardt, C. Hauswald, M. Wölz, L. Geelhaar, and O. Brandt, Luminous efficiency of axial $In_xGa_{1-x}N$/GaN nanowire heterostructures: Interplay of polarization and surface potentials, Nano Lett. **13**, 3298 (2013).

[71] O. Marquardt, L. Geelhaar, and O. Brandt, Impact of random dopant fluctuations on the electronic properties of $In_xGa_{1-x}N$/GaN axial nanowire heterostructures, Nano Lett. **15**, 4289 (2015).

[72] S. Sa, Closing the green gap, howpublished = https://www.energy.gov/sites/prod/files/2019/02/f59/hahn-gap_ssl-rd2019.pdf, note = Accessed: 2019-12-10.

[73] P. G. Eliseev, P. Perlin, J. Lee, and M. Osinski, "Blue" temperature-induced shift and band-tail emission in ingan-based light sources, Appl. Phys. Lett. **71**, 569 (1997).

[74] P. G. Eliseev, The red σ^2/kt spectral shift in partially disordered semiconductors, J. Appl. Phys. **93**, 5404 (2003).

[75] I. Vurgaftman and J. R. Meyer, Band parameters for nitrogen-containing semiconductors, J. Appl. Phys. **94**, 3675 (2003).

[76] S. Hammersley, D. Watson-Parris, P. Dawson, M. J. Godfrey, T. J. Badcock, M. J. Kappers, C. McAleese, R. A. Oliver, and C. J. Humphreys, The consequences of high injected carrier densities on carrier localization and efficiency droop InGaN/GaN quantum well structures, J. Appl. Phys. **111**, 083512 (2012).

[77] T. Wang, J. Bai, and S. Sakai, Influence of InGaN/GaN quantum-well structure on the performance of light-emitting diodes and laser diodes grown on sapphire substrates, J. Cryst. Growth **224**, 5 (2001).

[78] A. Alkauskas, C. E. Dreyer, J. L. Lyons, and C. G. Van de Walle, Role of excited states in shockley-read-hall recombination in wide-band-gap semiconductors, Phys. Rev. B **93**, 201304(R) (2016).

[79] E. Kioupakis, Q. Yan, and C. G. Van de Walle, Interplay of polarization fields and Auger recombination in the efficiency droop of nitride light-emitting diodes, Appl. Phys. Lett. **101**, 231107 (2012).

[80] E. Kioupakis, Q. Yan, and C. G. Van de Walle, Temperature and carrier-density dependence of auger and radiative recombination in nitride optoelectronic devices, New J. Phys. **15**, 125006 (2013).

[81] C. J. Humphreys, J. T. Griffiths, F. Tang, F. Oehler, S. D. Findlay, C. Zheng, J. Etheridge, T. L.Martin, P. A. J. Bagot, M. P. Moody, D. Sutherland, P. Dawson, S. Schulz, S. Zhang, W. Y. Fu, T. Zhu, M. J. Kappers, and R. A. Oliver, The atomic structure of polar and non-polar InGaN quantum wells and the green gap problem, Ultramicroscopy **176**, 93 (2017).

[82] M. Monavarian, A. Rashidi, and D. Feezell, A decade of nonpolar and semipolar III-Nitrides: A review of successes and challenges, Phys. Status Solidi A **216**, 1800628 (2019).

[83] G. A. Garrett, H. Shen, M. Wraback, A. Tyagi, M. C. Schmidt, J. S. Speck, S. P. DenBaars, and S. Nakamaura, Comparison of time-resolved photoluminescence from InGaN single quantum wells grown on nonpolar and semipolar bulk gan substrates, Phys. Stat. Solidi (c) **6**, S800 (2009).

[84] S. Marcinkevičius, K. M. Kelchner, L. Y. Kuritzky, S. Nakamura, S. P. DenBaars, and J. S. Speck, Photoexcited carrier recombination in wide m-plane InGaN/GaN quantum wells, Appl. Phys. Lett. **103**, 111107 (2013).

[85] A. M. Armstrong, B. N. Bryant, M. H. Crawford, D. D. Koleske, S. R. Lee, and J. J. Wierer, Jr., Defect-reduction mechanism for improving radiative efficiency in InGaN/GaN light-emitting diodes using InGaN underlayers, J. Appl. Phys. **117**, 134501 (2015).

[86] G. Christian, M. Kappers, F. Massabuau, C. Humphreys, R. Oliver, and P. Dawson, Effects of a si-doped ingan underlayer on the optical properties of InGaN/GaN quantum well structures with different numbers of quantum wells, Materials **9**, 1736 (2018).